nature

https://doi.org/10.1038/s41586-025-09412-1

Accelerated Article Preview

Pre-rRNA spatial distribution and functional organization of the nucleolus

Received: 31 October 2024

Accepted: 15 July 2025

Accelerated Article Preview

Cite this article as: Pan, Y.-H. et al. Pre-rRNA spatial distribution and functional organization of the nucleolus. *Nature* https://doi.org/10.1038/s41586-025-09412-1 (2025)

Yu-Hang Pan, Lin Shan, Yu-Yao Zhang, Zheng-Hu Yang, Yuan Zhang, Shi-Meng Cao, Xiao-Qi Liu, Jun Zhang, Li Yang & Ling-Ling Chen

Pre-rRNA spatial distribution and functional organization of the nucleolus

Yu-Hang Pan[1,6], Lin Shan[1,6], Yu-Yao Zhang[2,6], Zheng-Hu Yang[1,3], Yuan Zhang[1], Shi-Meng Cao[1], Xiao-Qi Liu[1], Jun Zhang[1], Li Yang[2], and Ling-Ling Chen[1,3,4,5*]

[1]State Key Laboratory of RNA Innovation, Science and Engineering, New Cornerstone Science Laboratory, CAS Center for Excellence in Molecular Cell Science, Shanghai Institute of Biochemistry and Cell Biology, University of Chinese Academy of Sciences, Chinese Academy of Sciences, Shanghai, China

[2]Center for Molecular Medicine, Children's Hospital, Fudan University and Shanghai Key Laboratory of Medical Epigenetics, International Laboratory of Medical Epigenetics and Metabolism, Ministry of Science and Technology, Institutes of Biomedical Sciences, Fudan University, Shanghai, China

[3]School of Life Science and Technology, ShanghaiTech University, Shanghai, China

[4]School of Life Science and Biotechnology, Shanghai Jiao Tong University, Shanghai 200240, China

[5]Shanghai Academy of Natural Sciences (SANS), Shanghai, China

[6]These authors contributed equally: Yu-Hang Pan, Lin Shan, Yu-Yao Zhang

[*]Correspondence: linglingchen@sibcb.ac.cn (L.-L.C.)

Summary

The multi-layered nucleolus serves as the primary site of ribosome biogenesis[1,2], where successive maturation of small (SSU)[3,4] and large (LSU)[5] ribosomal subunit precursors occur. However, the spatio-functional relationship between pre-rRNA processing and nucleolar substructures and how this adapts to changing cellular physiological demands have remained incompletely understood[6,7]. Here, our spatiotemporal analyses revealed a compartment-specific ribosomal subunit processing in human nucleoli, with SSU processomes maintained in fibrillar center/dense fibrillar component/periphery dense fibrillar component (FC/DFC/PDFC) domains while LSU pre-rRNAs largely transited to PDFC/granular component (GC) regions. Slow proliferating cells exhibited unexpected 5' external transcribed space (5' ETS)-centered SSU processing impairment, accompanied by FC/DFC structural remodeling and retarded SSU outflux. Direct 5' ETS processing perturbation at least partially recapitulated these FC/DFC alterations, supporting the functional interdependence between SSU processing and nucleolar architecture. Notably, anamniote bipartite nucleoli with merged FC/DFC compartments[8,9] exhibited distinct 5' ETS distribution and slower pre-rRNA flux compared to multi-layered nucleoli in amniotes. Introducing a FC/DFC interface to bipartite nucleoli enhanced processing efficiency, indicating that evolutionary emergence of nested FC/DFC may have optimized pre-rRNA processing. Collectively, depicting the spatiotemporal distribution of pre-rRNAs revealed an essential role of 5' ETS-centered SSU processing in maintaining nucleolar substructures and suggested a possible evolutionary advantage of the multi-layered structure in amniotes.

Main

The mammalian nucleolus is spatially organized into four nested layers[2,10], each plays a distinct role in ribosome production[1,10]. In mammals, 18S, 5.8S and 28S ribosomal RNAs (rRNAs) are transcribed as a single 47S pre-rRNA, approximately 13

kb in length[11]. Transcription by RNA polymerase I (Pol I) occurs at the FC/DFC border[12,13], after which the 47S pre-rRNA moves outward across each nucleolar layer, ultimately forming SSU[3,4] and LSU[5] in the GC[1,14]. The major precursor of SSU pre-rRNA is 30S, flanked by the 5' external and internal transcribed spacers (ETS and ITS1), while the LSU precursor is mainly 32S pre-rRNA, producing 5.8S and 28S rRNAs (Extended Data Fig. 1a). Given that the 47S pre-rRNA would span roughly 4~10 μm if fully extended[15], it must fold considerably to fit within the much smaller nucleolus, where the FC region measures around 150 nm and the FC-DFC region is ~400 nm in diameter[2,12]. This suggests that pre-rRNAs and interacting proteins undergo substantial compaction during ribosome assembly.

Specifically, nascent pre-rRNA is translocated to the DFC, where it undergoes chemical modifications and early cleavages at 5' and 3' ends[12,16]. Classic models propose that subsequent processing in the GC removes ETSs and ITSs to produce SSU and LSU[6,7] (Fig. 1a; Extended Data Fig. 1a). Although supported by extensive correlative evidence over decades, *in situ* studies have remained limited due to technical constraints inherent to conventional imaging and biochemical approaches[6,7,11]. Our recent imaging studies revealed a spatial localization of pre-rRNAs[1,5], which prompted us to examine their processing dynamics within the nucleolar substructures. Intriguingly, unlike the multi-layered mammalian nucleolus, anamniotes such as zebrafish possess a bipartite nucleolus with a single merged FC/DFC, named the fibrillar zone (FZ)[8,9]. The evolutionary expansion of the 5' ETS and ITS2 regions[17] implies a potential need for more efficient processing system in the multi-layered nucleolar organization. However, it has remained unclear whether pre-rRNA spatial processing in bipartite nucleoli differs from that in mammals, and whether this relates to the emergence of multi-layered nucleoli.

Here, we dissected the spatiotemporal processing of pre-rRNA intermediates, revealing an unexpected segregation of SSU and LSU pre-rRNAs in human nucleoli.

Critically, such spatial segmentation enhanced pre-rRNA processing efficiency, and the 5' ETS-centered SSU processing was key for maintaining nested FC/DFC subdomains. Compared to multi-layered nucleoli, bipartite nucleoli in anamniote cells showed much slower pre-rRNA outflux, implying a possible evolutionary benefit of the more complex nucleolar organization for processing efficiency in amniotes.

Nucleolar distribution of pre-rRNA

To understand how multi-step pre-rRNA processing and transport align with nucleolar organization, we designed smFISH probe sets targeting specific pre-rRNA intermediates, each validated by Northern Blotting (NB) (Extended Data Fig. 1b-f). Probes targeting 5' ETS-1 and 3' ETS recognized 47S pre-rRNA (Fig. 1a; Extended Data Fig. 1c). Structured illumination microscopy (SIM) imaging revealed that the 5' ETS-1-recognized pre-rRNA localized within the DFC, while the 3' ETS-targeted pre-rRNA enriched near the DFC/PDFC boundary (Fig. 1a), confirming previous observations[2,12] and suggesting distinct pre-rRNA processing zones (Extended Data Fig. 1a). Probes targeting ITS1 site 2, which separates the 18S rRNA (associated with SSU) from the 5.8S and 28S rRNAs (associated with LSU)[11] (Fig. 1b; Extended Data Fig. 1b), detected 47S to 41S pre-rRNAs, supported by NB (Extended Data Fig. 1d). smFISH showed that ITS1 signals were within and closely surrounding the DFC (Fig. 1c; Extended Data Fig. 1g), suggesting that SSU processing may precede the release of LSU sequences to downstream layers.

Next, to better understand the nucleolar distribution of different SSU-associated intermediates, such as 47S, 41S, 34S and 30S, we focused on the 5' ETS, the major component of SSU pre-rRNAs[18]. The 5' ETS region can be divided into three segments according to its cleavage sites: 5' ETS-1 (from the 5'-end to site 01) (Fig. 1a), 5' ETS-2 (site 01 to A0), and 5' ETS-3 (site A0 to 1)[19] (Extended Data Fig. 1b). Notably, 5' ETS moved toward the DFC as it is transcribed[12] (Fig. 1a). 5' ETS-2 signals extended from

the FC to the PDFC, whereas 5' ETS-3 signals were confined to the FC (Fig. 1b, d). This reflected a spatially distinct distribution of 5' ETS segments, which extended previous observations[3,12]. NB results confirmed these probe sets mostly detected 47S and 30S pre-rRNAs (Extended Data Fig. 1e), supporting their association with intact SSU pre-rRNAs rather than cleaved fragments. Together, these distribution patterns (Fig. 1a, c, d; Extended Data Fig. 1c, d, e, g) indicated that 47S and 30S pre-rRNAs-containing SSU processome assembly[20] mainly distributed from the FC to the PDFC. In contrast, probe sets targeting ITS2 (Fig. 1e; Extended Data Fig. 1f, h) revealed that LSU-associated pre-rRNA intermediates[11] (32S and 12S) were localized in the PDFC and the GC, suggesting that LSU processing and assembly predominantly occur in the outer nucleolar regions.

We further examined several essential snoRNAs that base-pair with different pre-rRNAs regions during processing[21]. U17A snoRNA, promotes 18S rRNA maturation at its 5' end[22], was enriched in the DFC (Fig. 1f). U13 and E2 snoRNAs[23], which interact with the 3' end of 18S rRNA, were also localized to the DFC (Extended Data Fig. 1i, j), substantiating the SSU pre-rRNA localization patterns (Fig. 1b-d). In contrast, U8 snoRNA, which assists in the processing of both 5'- and 3'-ends of 5.8S/28S rRNA precursors[24], was localized to the DFC/PDFC boundary, aligning with its LSU-related roles (Fig. 1e, f). These observations aligned with the patterns detected by the different ETS and ITS probes discussed above (Fig. 1a-e).

The spatial distribution of all key pre-rRNA intermediates within each sub-nucleolar domain is summarized in Fig. 1g.

Spatiotemporal pattern of nascent rRNA

To track dynamics of pre-rRNA intermediates and associated ribosomal subunits, we performed pulse-chase labeling incorporating 5-ethynyl uridine (5-EU) into nascent RNAs[25-28] (Extended Data Fig. 2a). Given the rapid transcription and processing of pre-

rRNAs[29], we pulse-labeled cells for 10 minutes (min) to ensure homogeneous nascent labeling, followed by 0-60 min chase at 10 min intervals before fixation (Extended Data Fig. 2a). After fluorescent conjugation via click chemistry, nascent RNAs were visualized by SIM, with FBL and B23 marking the DFC and GC, respectively (Fig. 1h).

Pulse-chase imaging (Fig. 1h) revealed that nascent pre-rRNAs progressively move outward from the transcription sites at the FC/DFC border. Quantitative analysis of the pre-rRNA signal intensities showed a steady outward flux along the radial axis of sub-nucleolar compartments over time (Extended Data Fig. 2b). This migration had an estimated velocity of ~1 Å/s across sub-compartments (Extended Data Fig. 2b, c), in agreement with a previous study[14].

As nascent pre-rRNAs move outward to the GC, they dispersed across larger volumes, lowering their spatial density (Extended Data Fig. 2d). Consequently, while the linear migration speed remained constant at ~1 Å/s, the relative diffusion flux declined in the outer nucleolar regions due to sparser pre-rRNA distributions (Fig. 1i; Extended Data Fig. 2d). The more crowded, smaller-volume inner nucleolar regions sustained higher diffusion flux (Fig. 1i). This pattern corresponded to a faster outflux of SSU pre-rRNAs from FC/DFC region within 30 min, followed by entry into the GC regions for LSU pre-rRNA processing after another 30 min (Fig. 1g, h).

SSU and LSU spatiotemporal separation

To dissect the temporal progression of pre-rRNA maturation, we next performed 5-EU-conjugated biotin pull-down of proteins bound to nascent pre-rRNAs at 0 min, 30 min, 60 min, followed by mass spectrometry (MS) analysis (Fig. 1j; Extended Data Fig. 2a, 3a-c). In agreement with the radial outflux of nascent rRNAs (Fig. 1h), FC proteins prominently bound to nascent pre-rRNAs at the initial 0 min chase stage, while DFC and PDFC proteins predominantly bound at the 30 min chase, and GC proteins at 60 min (Extended Data Fig. 3b), underscoring the sequential spatial progression of pre-

rRNA processing. SSU-associated components were enriched at early time points, while LSU-associated components peaked at 60 min (Fig. 1j; Extended Data Fig. 3c).

During early stages (0-30 min), nascent pre-rRNAs localized at the inner nucleolar regions ranging from the FC to the PDFC (Fig. 1h), covering a radius of ~250 nm (Extended Data Fig. 2b), suggesting rapid co-transcriptional[12] SSU processing (Fig. 1c, d, g, h). LSU-associated proteins exhibited peak enrichment at 60 min (Fig. 1j; Extended Data Fig. 3c), coinciding with pre-rRNAs reaching the GC at a radial distance of ~450 nm (Fig. 1h; Extended Data Fig. 2b), consistent with delayed LSU precursor processing (Fig. 1e, g). In comparison, SSU maturation involving 18S rRNA precursors (Fig. 1a-d; Extended Data Fig. 1g, 3c) showed a more complex spatial pattern than the LSU and 28S rRNA pathway (Fig. 1e; Extended Data Fig. 1h, 3c).

Supporting our observations, recent 4-thio-uridine (4sU)[30] pulse-chase interactome data similarly demonstrated sequential binding of FC, DFC, and PDFC proteins[2] to nascent pre-rRNAs within 40 min, and GC proteins thereafter (Extended Data Fig. 3d). The radial localization patterns identified by MS were validated by assessing established nucleolar protein[2] distribution patterns at corresponding chase intervals (0, 30, 60 min) via Western Blotting (WB) (Extended Data Fig. 3e, f), revealing sequential enrichment of RPA194 (FC) at 0 min, FBL (DFC) and DDX21 (PDFC) at 30 min, and B23 (GC) at 60 min. These results were consistent with the stepwise progression of pre-rRNA maturation (Extended Data Fig. 3e, f).

Collectively, these spatiotemporal profiles of SSU and LSU processing (Fig. 1g-j) add a spatially resolved dimension to the previous biochemical understanding of ribosomal assembly[4,8]. SSU processing, including 5' ETS and 30S pre-rRNAs, occurs predominantly from FC to PDFC regions, while LSU processing, involving 32S pre-rRNAs, proceeds from PDFC towards GC (Fig. 1k; Extended Data Fig. 3g).

Cell state impacts SSU pre-rRNA pattern

Given the distinct spatial organization of pre-rRNA processing, we asked whether cell state-dependent changes in proliferation would influence nucleolar sub-structures and SSU pre-rRNA dynamics. We compared the rapidly dividing human pluripotent stem cells (H9) with differentiated post-mitotic, slowly proliferating arcuate neurons and human SH-SY5Y neuroblastoma cells[31]. Neuronal cells have limited proliferation capacity, whose nucleoli underwent striking re-organization starting at the 2nd day of differentiation (Fig. 2a; Extended Data Fig. 4a). In rapidly proliferating H9 (Fig. 2a, b) and HeLa cells (Fig. 2c, d), individual nucleoli were composed of several dozen FC/DFC units, whereas in differentiated arcuate neurons and SH-SY5Y cells, the nucleolar volume was reduced with only single digit numbers of FC/DFC units (Fig. 2a-d). However, arcuate neurons and SH-SH5Y cells showed generally enlarged individual FC volumes, compared to H9 and HeLa cells (Fig. 2a-d; Extended Data Fig. 4b, c). Of note, the overall multi-layered nucleolar sub-structures persisted throughout differentiation (Extended Data Fig. 4c).

A potential functional-relevant change accompanying this morphological remodeling in FC/DFC was a shift in the spatial distribution of SSU pre-rRNAs (Fig. 1g-j). In H9 and HeLa cells, smFISH signals targeting the 5' ETS-3 region, representing early-stage SSU precursors, were enriched in the innermost FC (Fig. 2e and Fig. 1d). However, in arcuate neurons and SH-SY5Y cells, these signals were displaced outward to DFC–PDFC regions (Fig. 2e). In contrast, localization of other pre-rRNA segments, including SSU-associated 5' ETS-1 and ITS1 (Extended Data Fig. 5) and LSU-associated ITS2 and 3' ETS (Extended Data Fig. 6) remained largely unchanged, suggesting a selective disruption in 5' ETS-3 processing and localization corresponding to cellular status.

Slow growth hinders 5' ETS processing

Notably, these 5' ETS-3 localization changes (Fig. 1d, 2e) were related to pre-rRNA processing (Fig. 2f-h). In differentiated neurons, we observed by NB a roughly two-fold increase in 30S/47S ratio, here referring to the abundance of the 30S SSU precursor relative to the primary 47S transcript (Fig. 2f, g), indicating an increased accumulation of 30S pre-rRNA and inefficient 5' ETS cleavage, a critical event during SSU pre-rRNA processing. Similar observations were found in SH-SY5Y cells, which also showed a two-fold increased 30S/47S ratio compared to that in HeLa cells (Fig. 2h). In contrast, the LSU-associated 32S/47S and 12S/47S ratios remained unchanged in both arcuate neurons and SH-SY5Y cells (Fig. 2f-h), indicating that LSU pre-rRNA processing is not similarly affected. The increased accumulation of 30S pre-rRNA correlated with the outward redistribution of 5' ETS-3 smFISH signals from the FC to the DFC–PDFC in these cells (Fig. 2e-h), supporting a model in which impaired cleavage at the 5' ETS leads to premature export of unprocessed SSU precursors.

These findings suggested that the proliferation-dependent pre-rRNA processing is tightly linked to the spatial organization of SSU maturation within the nucleolar subdomains. These results also indicated that the inefficient 5' ETS processing likely represents a hallmark of slowly proliferating cells, which is selectively associated with disrupted SSU but not LSU pre-rRNA processing. (Fig. 2f-h).

Slow growth reduces FC/DFC interface

Along with the altered SSU pre-rRNA processing (Fig. 2f-h), the nucleolus underwent a marked re-organization (Fig. 2a-d). Given that 5' ETS processing of pre-rRNAs occurs across the DFC (Fig. 1g) and is accompanied with an altered sub-nucleolar FC/DFC structure (Fig. 2a-d), we hypothesized that inefficient 5' ETS processing is accompanied by an altered FC/DFC organization. To test this idea, we analyzed the Relative FC/DFC interface as one parameter to evaluate the change of individual FC/DFC substructures. Since FC/DFC interface is essential for SSU pre-

rRNA processing (Fig. 1d), we reasoned that the contact area between the surfaces of FC and DFC might be an indicator of altered FC/DFC substructure (Fig. 2i).

To minimize bias caused by variations in nucleolus size across cell types, we normalized the FC/DFC contact area to the respective FC volume to generate a Relative FC/DFC interface (Extended Data Fig. 4d). Theoretically, by simplifying the FC/DFC units into spherical structures, the Relative FC/DFC interface was inversely proportional to individual FC radius (Extended Data Fig. 4d). The FC and DFC regions were labeled with RPA194 (the largest subunit of Pol I) and FBL, respectively, and we quantified the Relative FC/DFC interface in cells varying in proliferation rates (Fig. 2i, see Methods). Our results showed that neurons with slow proliferation displayed a reduced Relative FC/DFC interface (Fig. 2i). Importantly, the experimentally validated Relative FC/DFC interface in different cell types was inversely proportional to the FC radius, consistent with our prediction (Fig. 2b, d, i; Extended Data Fig. 4d).

Aligned with the observed correlation between the retarded 5' ETS processing (Fig. 2f-h) and reduced Relative FC/DFC interfaces in post-mitotic cells (Fig. 2i), D30 arcuate neuron and SH-SY5Y cells exhibited fewer transcriptionally active rDNA units and increased puncta of inactive rDNA repeats (Extended Data Fig. 7a, b). RNA-seq analysis further revealed that a large subset of pre-rRNA processing factors (387 of 525 analyzed) exhibited reduced expression in D30 arcuate neurons relative to H9 cells (Extended Data Fig. 7c). Complementary pulse-chase MS analyses (Extended Data Fig. 2a) showed a delayed binding duration of SSU, but not LSU, ribosomal precursors in SH-SY5Y cells (Extended Data Fig. 7d-f) compared to that in HeLa cells (Extended Data Fig. 3c; 7f), indicating a retarded maturation kinetics of SSU processome in SH-SY5Y cells. These findings together highlighted a structural–functional coupling between nucleolar sub-architecture (Fig. 2a-e, i), pre-rRNA processing (Fig. 2f-h), and ribosome output (Extended Data Fig. 7d–f) in response to reduced cell proliferation status (Fig. 2j). Remarkably, these slow growing cells with remodeled FC/DFC

architectures (Fig. 2a-e) also exhibited reduced nascent pre-rRNA outflux, approximately 5-fold and 2-fold, in D30 arcuate neurons and SH-SY5Y cells, compared to H9 and HeLa cells, respectively (Fig. 3a, b; Extended Data Fig. 7g), further supporting the notion that SSU pre-rRNA processing is tightly linked to nucleolar subcompartment organization.

5' ETS disruption reshapes FC/DFC units

To directly evaluate whether the naturally occurring retarded SSU pre-rRNA processing in post-mitotic cells (Fig. 2f-h; Fig. 3a, b) is key for maintaining appropriate FC/DFC architectures (Fig. 2i, j), we perturbed the early 5' ETS cleavage using antisense oligonucleotides (ASOs) targeting cleavage sites A0 and 1 (Fig. 3c). ASOs targeting LSU pre-rRNA processing sites, ASO-U8 site and ASO-3' ETS, were designed as controls (Fig. 3c). NB analyses revealed disrupted SSU pre-rRNA processing upon ASO-Site A0 and ASO-Site 1 treatments, with accumulation of 30S rRNA precursors, although the effect was less pronounced with ASO-Site 1 treatment in HeLa cells (Fig. 3c, d). LSU pre-rRNA processing was also successfully disrupted by ASO-U8 and ASO-3' ETS treatments, resulting in aberrant intermediates and reduced 12S pre-rRNA levels (Fig. 3d).

Imaging analyses revealed that upon SSU pre-rRNA processing perturbation with ASO-Site A0, 5' ETS-3 signals became diffuse and localized to outer DFC regions (Extended Data Fig. 8a). In contrast, these signals still remained FC-enriched in ASO-scramble or ASO-3' ETS treated cells (Extended Data Fig. 8a). To assess whether such ASO-induced perturbations in pre-rRNA processing and distribution (Fig. 3d; Extended Data Fig. 8a) would alter nucleolar morphology, we treated mRuby3-DKC1 (DFC) /BFP-B23 (GC) knock-in HeLa cells with ASOs and performed IF imaging together with anti-RPA194 (FC). The ASO-Site A0 treatment induced strikingly reorganization of FC/DFC units, with most nucleoli (>50%) showing enlarged FC/DFC structures, and

a subset (~20%) exhibiting fragmentation (Fig. 3e; Extended Data Fig. 8b-d). This was accompanied by measurable changes in FC/DFC architectures, including reduced Relative FC/DFC interface, fewer FCs per nucleolus, and increased FC volume (Fig. 3f).

The ASO-Site 1 treatment similarly altered FC/DFC units, though with milder effects, such as reduced proportions of enlarged or fragmented FC/DFC architectures (Extended Data Fig. 8b-d; Fig. 3f), consistent with its weaker perturbation of SSU pre-rRNA processing compared to the ASO-Site A0 treatment (Fig. 3d). Nonetheless, these ASO-mediated SSU processing inhibition-induced subnucleolar reorganization patterns (Fig. 3c-f) largely phenocopied the enlarged nucleolar morphology observed in post-mitotic cells (Fig. 2a-d), underscoring the importance of efficient SSU processing in maintaining nucleolar FC/DFC structures. In contrast, control treatments targeting LSU pre-rRNA processing (ASO-U8 or ASO-3' ETS; Fig. 3c, d) showed no significant substructural changes (Fig. 3e, f), consistent with LSU pre-rRNA processing occurring primarily in the GC (Fig. 1e-g).

SSU pattern shifts in bipartite nucleoli

Since impaired 5' ETS processing disrupted the FC/DFC organization in human cells (Fig. 3e, f), we asked whether the spatial distribution of pre-rRNA segments would differ in naturally bipartite nucleoli containing a single merged FC/DFC structure (FZ), as observed in zebrafish fibroblast cells (ZF4) and embryos. Indeed, zebrafish cells showed distinct 5' ETS signal distribution patterns from that in human nucleoli (Fig. 1g, 4a). These 5' ETS signals did not localize within the inner region of Fbl, but overlapping with Fbl (Fig. 4a; Extended Data Fig. 9a). While ITS2 signals predominantly maintained their peripheral Fbl localization in bipartite nucleoli (Fig. 4a; Extended Data Fig. 9a), similar to their tripartite nucleolar distribution (Fig. 1g). These findings aligned with our human cell perturbation experiments showing 5' ETS-

centered processing sustained the Relative FC/DFC interface integrity (Fig. 2i, j; Extended Data Fig. 4d), and the lack of FC/DFC organization in zebrafish FZ appeared consistent with this functional relationship (Fig. 4a, b; Extended Data Fig. 9a).

However, the much shorter zebrafish 5' ETS (~1 kb[32] compared to human ~3.6 kb, Extended Data Fig. 1a)[3] might reduce spatial demands for SSU processing, potentially favoring both simplified pre-rRNA distribution and bipartite nucleolar organization. Thus, we attempted to determine whether this simpler SSU distribution and organization (Fig. 4a, b) could impact pre-rRNA processing dynamics by measuring nascent rRNA flux in zebrafish embryos.

Multi-layered nucleoli boost rRNA flux

We first performed 5-EU pulse-chase labeling in zebrafish embryos. *EGFP-Fbl* mRNA was microinjected into 1-cell stage embryos to label the FZ. At approximately 3 hr post-fertilization (hpf), coinciding with zygotic genome activation (ZGA) to minimize the maternal effect, we injected 5-EU to label nascent pre-rRNAs. Embryos were then fixed at defined intervals (Fig. 4c). Nascent pre-rRNAs accumulate within the Fbl-marked FZ after 30 min of labeling, with gradual movement across the FZ (~1 μm border) into the granular zone (GZ) over 60-90 min, but rarely exceeding the 3 μm boundary (Fig. 4d; Extended Data Fig. 9b). Even after prolonged tracing (180 min), labeled nascent pre-rRNAs persisted in the transcriptionally active inner nucleolar region, showing slow pre-rRNA flux in zebrafish nucleoli (Fig. 4d; Extended Data Fig. 9b). By contrast, parallel experiments in HeLa cells showed that nascent pre-rRNAs rapidly migrated from the FC border to GC within similar time frames (Fig. 4d, e; Extended Data Fig. 9b, c). Of note, the intensity of the Pol II transcribed nascent RNAs kept increasing over the 180 min 5-EU labeling, excluding a possible 5-EU exhaustion-caused signal reduction of nascent pre-rRNAs within the innermost FC region in HeLa cells (Extended Data Fig. 9d, e). Similar slow nascent pre-rRNA flux was also observed

in ZF4 cells (Extended Data Fig. 10a), suggesting that the bipartite nucleolar architecture intrinsically restricted pre-rRNA movement.

Quantitative analyses revealed the comparable radial migration velocity across the GZ (~1 Å/s) between zebrafish and HeLa cells (Fig. 4f; Extended Data Fig. 2c), while the overall outflux rate of pre-rRNAs across the entire FZ was approximately seven-fold lower in zebrafish cells compared to HeLa cells (Fig. 4f, g; Extended Data Fig. 10b, c). This difference indicated that pre-rRNA processing in bipartite nucleoli took substantially longer time to reach the FZ boundary than those in multi-layered nucleoli to reach the border of DFC (Fig. 4g). Of note, zebrafish and human cells were cultured under their respective temperatures, but such temperature difference only mildly affects enzymatic reactions[33,34], unlikely representing a major contributor to the observed reduction of pre-rRNA outflux (Fig. 4f, g).

Finally, introducing the human TCOF1 to ZF4 cells to transform bipartite nucleoli into the mammalian tripartite-like structures[35] led to an accelerated outward flux of nascent pre-rRNAs (Extended Data Fig. 10d, e), highlighting the notion that multi-layered nucleolar architecture supports more efficient ribosome biogenesis.

Discussion

The nucleolus is among the most well-studied nuclear bodies, yet the mechanisms behind its multi-layered organization and how this structure enables efficient pre-rRNA processing remain elusive. This knowledge gap persisted due to inadequate tools to link pre-rRNA distribution with processing. Using multimodal high-resolution imaging, spatiotemporal MS, and mathematic modeling, we uncovered asynchronous maturation of SSU and LSU in nucleolar subdomains (Fig. 1), refining the uniform DFC/GC transit model[6,7] to reveal compartmentalized regulation.

Notably, direct perturbation of 5' ETS processing by ASOs led to enlarged or fragmented FC/DFC substructures (Fig. 3), suggesting critical feedback between processing activity and subcompartment integrity. This relationship was supported by synthetic nucleolar systems, where impaired SSU processing similarly disrupted FC/DFC layering[36]. Such a dynamic reorganization of FC/DFC architectures was correlated with altered pre-rRNA SSU processing in response to cellular ribosome demands (Fig. 2), indicating a previously underappreciated structure–function interdependence at the subnucleolar level. Given essential functions of nucleoli in supporting cell growth, selectively modulating SSU pre-rRNA processing may offer a potential therapeutic strategy for diseases with dysregulated proliferation.

Finally, this efficient and highly organized SSU processing appears to necessitate the emergence of the multi-layered nucleolus. Zebrafish cells appeared to process pre-rRNA less efficiently compared to those in amniotes (Fig. 4), indicating the presence of FC/DFC subdomains in amniotes may provide an advantage by enhancing SSU pre-rRNA processing during the evolutionary emergence of the multi-layered nucleolus. Future studies are needed to deepen the molecular mechanisms underlying this model (Fig. 4h), investigate how multi-layered nucleoli co-evolve with ribosome biogenesis, and evaluate additional factors, such as temperature, cell cycle and metabolic activity[37,38], to better address species-specific variations in ribosome biogenesis.

References

1 Lafontaine, D. L. J., Riback, J. A., Bascetin, R. & Brangwynne, C. P. The nucleolus as a multiphase liquid condensate. *Nat Rev Mol Cell Biol* **22**, 165-182 (2021). https://doi.org:10.1038/s41580-020-0272-6

2 Shan, L. *et al.* Nucleolar URB1 ensures 3' ETS rRNA removal to prevent exosome surveillance. *Nature* **615**, 526-534 (2023). https://doi.org:10.1038/s41586-023-05767-5

3 Singh, S., Vanden Broeck, A., Miller, L., Chaker-Margot, M. & Klinge, S. Nucleolar maturation of the human small subunit processome. *Science* **373**, eabj5338 (2021). https://doi.org:10.1126/science.abj5338

4 Barandun, J., Hunziker, M. & Klinge, S. Assembly and structure of the SSU processome-a nucleolar precursor of the small ribosomal subunit. *Curr Opin Struct Biol* **49**, 85-93 (2018). https://doi.org:10.1016/j.sbi.2018.01.008

5 Kater, L. *et al.* Visualizing the Assembly Pathway of Nucleolar Pre-60S Ribosomes. *Cell* **171**, 1599-1610 e1514 (2017). https://doi.org:10.1016/j.cell.2017.11.039

6 Erdmann, P. S. *et al.* In situ cryo-electron tomography reveals gradient organization of ribosome biogenesis in intact nucleoli. *Nat Commun* **12**, 5364 (2021). https://doi.org:10.1038/s41467-021-25413-w

7 Klinge, S. & Woolford, J. L., Jr. Ribosome assembly coming into focus. *Nat Rev Mol Cell Biol* **20**, 116-131 (2019). https://doi.org:10.1038/s41580-018-0078-y

8 Jaberi-Lashkari, N., Lee, B., Aryan, F. & Calo, E. An evolutionarily nascent architecture underlying the formation and emergence of biomolecular condensates. *Cell Reports* **42** (2023). https://doi.org:10.1016/j.celrep.2023.112955

9 Thiry, M., Lamaye, F. & Lafontaine, D. L. J. The nucleolus: When 2 became 3. *Nucleus* **2**, 289-293 (2014). https://doi.org:10.4161/nucl.2.4.16806

10 Dörner, K. & Hondele, M. The Story of RNA Unfolded: The Molecular Function of DEAD- and DExH-Box ATPases and Their Complex Relationship with Membraneless Organelles. *Annual Review of Biochemistry* **93**, 79-108 (2024). https://doi.org:10.1146/annurev-biochem-052521-121259

11 Tafforeau, L. *et al.* The complexity of human ribosome biogenesis revealed by systematic nucleolar screening of Pre-rRNA processing factors. *Mol Cell* **51**, 539-551 (2013). https://doi.org:10.1016/j.molcel.2013.08.011

12 Yao, R. W. *et al.* Nascent Pre-rRNA Sorting via Phase Separation Drives the Assembly of Dense Fibrillar Components in the Human Nucleolus. *Mol Cell* **76**, 767-783 e711 (2019). https://doi.org:10.1016/j.molcel.2019.08.014

13 Thiry, M., Cheutin, T., O'Donohue, M.-F., Kaplan, H. & Ploton, D. Dynamics and three-dimensional localization of ribosomal RNA within the nucleolus. *Rna* **6**, 1750-1761 (2000). https://doi.org:10.1017/s1355838200001564

14 Riback, J. A. *et al.* Viscoelasticity and advective flow of RNA underlies nucleolar form and function. *Mol Cell* **83**, 3095-3107 e3099 (2023). https://doi.org:10.1016/j.molcel.2023.08.006

15 Newby Lambert, M. *et al.* Mg2+-Induced Compaction of Single RNA Molecules Monitored by Tethered Particle Microscopy. *Biophysical Journal* **90**, 3672-3685 (2006). https://doi.org:10.1529/biophysj.105.067793

16 Meier, U. T. The daunting task of modifying ribosomal RNA. *RNA* **28**, 1555-1557 (2022). https://doi.org:10.1261/rna.079391.122

17 Henras, A. K., Plisson-Chastang, C., O'Donohue, M. F., Chakraborty, A. & Gleizes, P. E. An overview of pre-ribosomal RNA processing in eukaryotes. *Wiley Interdiscip Rev RNA* **6**, 225-242 (2015). https://doi.org:10.1002/wrna.1269

18 Hunziker, M. *et al.* Conformational switches control early maturation of the eukaryotic small ribosomal subunit. *Elife* **8** (2019). https://doi.org:10.7554/eLife.45185

19 Mullineux, S. T. & Lafontaine, D. L. Mapping the cleavage sites on mammalian pre-rRNAs: where do we stand? *Biochimie* **94**, 1521-1532 (2012). https://doi.org:10.1016/j.biochi.2012.02.001

20 Vanden Broeck, A. & Klinge, S. An emerging mechanism for the maturation of the Small Subunit Processome. *Curr Opin Struct Biol* **73**, 102331 (2022). https://doi.org:10.1016/j.sbi.2022.102331

21 Enright, C. A., Maxwell, E. S., Eliceiri, G. L. & Sollner-Webb, B. 5'ETS rRNA processing facilitated by four small RNAs: U14, E3, U17, and U3. *RNA* **2**, 1094-1099 (1996).

22 Mishra, R. K. & Eliceiri, G. L. Three small nucleolar RNAs that are involved in ribosomal RNA precursor processing. *Proc Natl Acad Sci U S A* **94**, 4972-4977 (1997). https://doi.org:10.1073/pnas.94.10.4972

23 Rimoldi, O. J., Raghu, B., Nag, M. K. & Eliceiri, G. L. Three new small nucleolar RNAs that are psoralen cross-linked in vivo to unique regions of pre-rRNA. *Mol Cell Biol* **13**, 4382-4390 (1993). https://doi.org:10.1128/mcb.13.7.4382-4390.1993

24 Peculis, B. A. & Steitz, J. A. Disruption of U8 nucleolar snRNA inhibits 5.8S and 28S rRNA processing in the Xenopus oocyte. *Cell* **73**, 1233-1245 (1993). https://doi.org:10.1016/0092-8674(93)90651-6

25 Bao, X. *et al.* Capturing the interactome of newly transcribed RNA. *Nat Methods* **15**, 213-220 (2018). https://doi.org:10.1038/nmeth.4595

26 Jao, C. Y. & Salic, A. Exploring RNA transcription and turnover in vivo by using click chemistry. *Proc Natl Acad Sci U S A* **105**, 15779-15784 (2008). https://doi.org:10.1073/pnas.0808480105

27 Riback, J. A. *et al.* Viscoelasticity and advective flow of RNA underlies nucleolar form and function. *Molecular Cell* **83**, 3095-3107.e3099 (2023). https://doi.org:10.1016/j.molcel.2023.08.006

28 Thiry, M., Cheutin, T., O'Donohue, M. F., Kaplan, H. & Ploton, D. Dynamics and three-dimensional localization of ribosomal RNA within the nucleolus. *RNA* **6**, 1750-1761 (2000). https://doi.org:10.1017/s1355838200001564

29 Schneider, D. A. *et al.* Transcription elongation by RNA polymerase I is linked to efficient rRNA processing and ribosome assembly. *Mol Cell* **26**, 217-229 (2007). https://doi.org:10.1016/j.molcel.2007.04.007

30 Choi, Y. *et al.* Time-resolved profiling of RNA binding proteins throughout the mRNA life cycle. *Mol Cell* **84**, 1764-1782 e1710 (2024). https://doi.org:10.1016/j.molcel.2024.03.012

31 Huang, W. K. *et al.* Generation of hypothalamic arcuate organoids from human induced pluripotent stem cells. *Cell Stem Cell* **28**, 1657-1670 e1610 (2021). https://doi.org:10.1016/j.stem.2021.04.006

32 Locati, M. D. *et al.* Expression of distinct maternal and somatic 5.8S, 18S, and 28S rRNA types during zebrafish development. *RNA* **23**, 1188-1199 (2017). https://doi.org:10.1261/rna.061515.117

33 Shanmugam, T. *et al.* Dynamics and thermal sensitivity of rRNA maturation paths in plants. *Journal of Experimental Botany* (2021). https://doi.org:10.1093/jxb/erab434

34 Sharma, S. *et al.* A single N1-methyladenosine on the large ribosomal subunit rRNA impacts locally its structure and the translation of key metabolic enzymes. *Scientific Reports* **8** (2018). https://doi.org:10.1038/s41598-018-30383-z

35 Jaberi-Lashkari, N., Lee, B., Aryan, F. & Calo, E. An evolutionarily nascent architecture underlying the formation and emergence of biomolecular condensates. *Cell Rep*, 112955 (2023). https://doi.org:10.1016/j.celrep.2023.112955

36 Quinodoz, S. A. *et al.* Mapping and engineering RNA-driven architecture of the multiphase nucleolus. *Nature* (2025). https://doi.org:10.1038/s41586-025-09207-4

37 Badertscher, L. *et al.* Genome-wide RNAi Screening Identifies Protein Modules Required for 40S Subunit Synthesis in Human Cells. *Cell Rep* **13**, 2879-2891 (2015). https://doi.org:10.1016/j.celrep.2015.11.061

38 Kos, M. & Tollervey, D. Yeast pre-rRNA processing and modification occur cotranscriptionally. *Mol Cell* **37**, 809-820 (2010). https://doi.org:10.1016/j.molcel.2010.02.024

Methods

Cell culture

Human HeLa and SH-SY5Y cells were purchased from the American Type Culture Collection (ATCC; http://www.atcc.org) and were authenticated using STR profiling. Human H9 cells were purchased from WiCell. Zebrafish ZF4 cells were purchased from YaJi Biological. HeLa cells were maintained in DMEM, which was supplemented with 10% fetal bovine serum (FBS). H9 cells were maintained in DMEM/F-12 supplemented with 20% KnockOut Serum Replacement, 0.1 mM Glutamax, 0.1 mM non-essential amino acids and 0.1 mM mercaptoethanol and 4 ng/ml b-FGF and cultured with irradiated mouse embryonic fibroblast feeder cells with daily changed cultured medium and passaged weekly. SH-SY5Y cells were maintained in a 1:1 mixture of Eagle's Minimum Essential Medium and F12 Medium with 10% FBS. All cells were cultured at 37 °C in a 5% CO_2 cell culture incubator. ZF4 cells were maintained in DMEM:F12 medium with 10% FBS and were cultured at 28 °C in a 5% CO_2 cell culture incubator. All cells were routinely tested to exclude mycoplasma contamination.

Differentiation of H9 cells

Cell differentiation was performed as described before[39]. H9 cells were grown on 6-well plate coated with matrigel. The neuron differentiation procedure started when H9 cells reached 95% to 100% confluence. H9 cells were cultured in KSR medium with 100 ng/ml SHH (R&D Systems; cat. no. 1845-SH), 2 μM purmorphamine (Selleckchem; cat. no. S3042), 10 μM SB431542 (Selleckchem; cat. no. S1067), and 2.5 μM LDN-193189 (Selleckchem; cat. no. S2618) and the medium changed daily from day 1 to day 4. The medium was changed to KSR medium and N2 medium from 3:1, 1:1 to 1:3 ratio and supplemented with 100 ng/ml SHH, 2 μM purmorphamine, 10 μM SB431542, and 2.5 μM LDN-193189 from day 5 to day 7. On day 8, the medium was changed to N2 medium supplemented with 100 ng/ml SHH, 2 μM purmorphamine, 10 μM SB431542, and 2.5 μM LDN-193189. From day 9 to day 12, the cells were

cultured in N2 medium supplemented with 1× B-27 and 10 μM DAPT. The medium needed to be replaced daily. On day 10, we coated 0.01% poly-L-ornithine on new 10 cm dishes and the next day, aspirated poly-L-ornithine, washed the plates with sterile distilled water four times, added matrigel to each well, and incubated the plates overnight at 37°C. On day 12, the differentiated cells were treated with accutase for 8 min at 37°C, then added 2 ml N2 medium and detached all cells by repeatedly pipetting. After pelleting cells by centrifugation for 3 min at 800 rpm and aspirating the supernatant, N2 medium supplemented with B-27 and 10 μM ROCK inhibitor were used to suspend cell pallets. 6 million cells were seeded into every 10 cm dish coated with matrigel. From day 13 to day 16, the N2 medium supplemented with B-27 and 10 μM DAPT was replaced daily. From day 17, the medium was changed to N2 medium supplemented with B-27 and 20 ng/ml BDNF every two days until fully differentiated neurons were observed at day 30.

RNA isolation, Northern blotting (NB)

Total RNAs from the cultured cells were extracted with TRizol Reagent (Invitrogen) according to the manufacturer's protocol. The electrophoresis gels were imaged by Tanon Chemi Dog Ultra Imaging system. NB was carried out according to the manufacturer's protocol (DIG Northern Starter Kit, Roche) to examine pre-rRNAs. RNA was loaded on agarose gels and the Dig-labeled antisense probes were used. Probe sequences for northern blot are listed in Supplementary Table 1.

Western blotting (WB)

Nascent RNA-bound proteins were collected after treatments and resuspended in lysis buffer (1% NP-40, 0.5% sodium deoxycholate, 0.1% SDS, 150 mM NaCl, 50 mM Tris and 1× protease inhibitor cocktail, pH 8.0) for 10 min. After centrifugation, supernatants containing soluble proteins were resolved on polyacrylamide gel with 10% SDS and analyzed by WB with anti-RPA194 (Santa Cruz, 1:100 dilution), anti-FBL

(Abcam, 1:1,000 dilution), anti-DDX21 (ProteinTech, 1:1,000 dilution), anti-B23 (Santa Cruz, 1:100 dilution) or anti-ATCB (Sigma, 1:5,000 dilution) antibodies.

Single molecule RNA Fluorescence *in situ* Hybridization (smFISH)

All smFISH probes were designed via Stellaris Probe Designer and labeled with Cy3 on the 3' end. smFISH was carried out as described before [40]. In brief, cells were fixed with 4% PFA for 15 min, followed by permeabilization with 0.5% Triton X-100 for 10 min. Cells were incubated in 10% formamide/2× SSC for 10 min at room temperature followed by hybridization at 37 °C for 16 h. After hybridization, the cells were washed for 2 times with 10% formamide/2× SSC at 37 °C, each time for 30 min. Samples were mounted in VECTASHIELD antifade mounting medium (Vector Lab). Probe sequences for smFISH are listed in Supplementary Table 1.

Protein visualization

To detect protein localization by immunofluorescence in fixed cells, cells were seeded on High Performance No.1.5 18×18 mm glass coverslips and were fixed with 4% PFA for 15 min, followed by permeabilization with 0.5% Triton X-100 for 10 min. Then cells were blocked with 1% BSA for 1 hour at room temperature (RT). Primary antibodies were diluted with 1% BSA (FBL, Abcam, 1:300 dilution; RPA194, Santa Cruz, 1:50 dilution; B23, Santa Cruz, 1:50 dilution) and incubated for 1 hour at RT. After washing with 1× DPBS 3 times, fluorescent secondary antibodies (Goat anti-Mouse Secondary Antibody Alexa Fluor 555, Goat anti-Mouse Secondary Antibody Alexa Fluor 647, or Goat anti-Rabbit Secondary Antibody Alexa Fluor 488) were 1: 1000 diluted in 1% BSA and incubated for 1 hour at RT. Samples were mounted in VECTASHIELD antifade mounting medium (Vector Lab).

DNA Fluorescent in situ Hybridization (DNA FISH)

To detect rDNAs, cells were seeded on High Performance No.1.5 18×18mm glass coverslips and fixed with 4% PFA for 15 min, followed by permeabilization with 0.5%

Triton X-100 for 5 min, incubated at 37 °C for 1 hour with RNase A. Cells were then denatured at 80 °C for 10 min in prewarmed 2 × SSC and 70% deionized formamide. Next, cells were hybridized with the denatured DNA probes prepared from Nick Translation (Abbott) overnight. After hybridization, two washes of 10 min at 37 °C with 4 × SSC. To co-localize proteins, IF was performed as described above. Slides were mounted with Slowfade antifade reagent (Thermo Fisher).

Structured Illumination Microscopy (SIM) procedure

All SIM experiments were performed using commercialized Hessian-SIM, termed His-SIM (High Intelligent and Sensitive Microscope) equipped with a 100×/1.5NA oil immersion objective (Olympus) and commercialized Multi-SIM (Multimodality Structured Illumination Microscopy) imaging system (NanoInsights-Tech Co., Ltd.) equipped with a 100× 1.49 NA oil objective (Nikon CFI SR HP Apo). Image acquisition was carried out using IMAGER software (1.4.21c). SIM image stacks were captured with a z-distance of 0.1 μm or 0.2 μm with 5 phases, 3 angles, and 15 raw images per plane.

Confocal super-resolution microscopy

Confocal super-resolution microscope images were acquired with the Spinning disk Olympus IXplore SpinSR microscope equipped with Yokogawa CSU-W1 SoRa (50 μm and SoRa disks) and operated with cellSens Dmension Software (3.1) and with the Nikon AX/AX R microscope equipped with NSPARC.

Pulse-chase labeling combined with imaging

HeLa cells were cultured in the medium supplemented with 1 mM 5-EU (Beyotime) for 10 min. Then the medium was replaced with the fresh 5-EU-free medium. Next, cells were fixed at indicated time points with 4% PFA for 15 min, followed by permeabilization with 0.5% Triton X-100 for 10 min. The click reaction for nascent RNA labeling was carried out as described in the manufacturer's protocol (Thermo

Fisher C10642) with the following modifications: (1) the free copper (component C) and the copper protectant (component D) level in the reaction mix was medium (1:1); (2) the Alexa Fluor picolyl azide concentration was 1 μM; (3) cells were incubated with the reaction mixture for 30 min and was washed 3 times with DPBS. Finally, samples were mounted in VECTASHIELD antifade mounting medium (Vector Lab) for imaging.

Pulse-chase labeling combined with mass spectrometry (MS) analysis

The procedure was modified from previous publication [41]. Cells were seeded on 10-cm dishes to perform pulse-chase labeling until the confluence reaches 70-80%. ~1×10^7 cells for each replicate (per time point: 0, 30, 60 min chase) were used as sufficient materials for the subsequent procedures. Cells were pulse labeled with 5-EU (Beyotime) for 10 min at 37 °C with 5% CO_2. Then, cells were washed twice with 1× DPBS to remove the remnant 5-EU. Cells were then chased with 5-EU-free medium over different time points. Next, cells were crosslinked with 1% formaldehyde for 10 min at room temperature, followed by 125 mM glycine treatment to stop the crosslinking reaction. Cells were washed twice with 1× DPBS, and then permeabilized with 0.5 % Triton X-100 for 10 min at room temperature, followed by twice wash with 1× DPBS. The click reaction mix was prepared with 20 mM Tris-HCl (pH 7.5), 250 μM biotin picolyl azide (Sigma-Aldrich, 900912), 1 mM $CuSO_4$ (Sigma-Aldrich, 451657), 2 mM BTTAA (Vector Laboratories, CCT-1236), 1 mM aminoguanidine (Sigma-Aldrich, 396494), and 2.5 mM Sodium L-ascorbate (Sigma-Aldrich, 11140). 5-EU labeled nascent RNAs reacted with the mixture to conjugate biotin for 60 min at room temperature. Then the unbound biotin was washed out with 1× DPBS.

Cells were scraped, resuspended in 1 mL lysis buffer (20 mM Tris pH 7.5, 500 mM NaCl, 1 mM EDTA pH 8.0, 0.5 mM PMSF, 2 mM RVC, protease inhibitor cocktail (Roche)) followed by 5× 20s sonication with an interval of 1 min on ice. The supernatant was collected after centrifuging at 14000 rpm for 10 min at 4 °C. 100 μL

Dynabeads MyOne Streptavidin C1 beads (Invitrogen, 65002) were washed with 1 mL lysis buffer for three times, followed by blocking beads with 1% BSA and 20 μg/ml yeast tRNA for 1 h at 4 °C. Then the supernatant was incubated with the beads for 3 h at 4 °C, followed by washing with wash buffer 1 (20 mM Tris pH 7.5, 500 mM NaCl, 1 mM EDTA pH 8.0, 0.5% SDS, 0.5 mM PMSF, 2 mM RVC, protease inhibitor cocktail (Roche)), wash buffer 2 (20 mM Tris pH 7.5, 500 mM NaCl, 1 mM EDTA pH 8.0, 0.1% SDS, 0.5 mM PMSF, 2 mM RVC, protease inhibitor cocktail (Roche)), and wash buffer 3 (20 mM Tris pH 7.5, 200 mM NaCl, 1 mM EDTA pH 8.0, 5 mM DTT, 0.5 mM PMSF, 2 mM RVC, protease inhibitor cocktail (Roche)). Finally, the enriched protein samples were sent to Shanghai Applied Protein Technology for mass spectrometry analysis.

Mass spectrometry (MS) detection

MS analyses (Supplementary Table 2) were analyzed by two different mass spectrometers (Thermo Scientific and Bruker, see below). Only the eluted peptides of the rep 1 MS data in HeLa cells were analyzed using a Q-Exactive mass spectrometer (Thermo Scientific) employing the HCD (higher-energy Collisional Dissociation) fragmentation method with the electrospray ionization mass spectrometry (ESI-MS) for detection in a positive ion mode. The MS1 scan range was set from 300 to 1,800 m/z, with a resolution of 70,000 at 200 m/z. The automatic gain control (AGC) target was 1e6, and the maximum injection time (IT) was 50 ms. The dynamic exclusion time was set to 30.0s. For peptide fragmentation, the instrument was set to collect 20 MS scans following each full MS scan. The MS2 activation type was HCD, with an isolation window of 2 m/z. The MS2 resolution was 17,500 at 200 m/z. The Normalized Collision Energy (NCE) was set to 27eV, and the underfill ratio was 0.1%.

Peptide samples in other replicates in HeLa cells and all replicates in SH-SY5Y were analyzed on a timsTOF Pro mass spectrometer (Bruker) operated in positive ion mode. The ion source voltage was set to 1.5 kV, and both MS and MS/MS spectra were

acquired using the TOF (time-of-flight) analyzer. The mass range for detection was set to 100-1,700 m/z. Data were acquired in PASEF mode (Parallel Accumulation-Serial Fragmentation). For each MS1 survey scan, 8 PASEF MS/MS scans were acquired. The cycle time was 0.95s, and MS/MS spectra were collected for precursors with charge states ranging from +0 to +5. A dynamic exclusion time of 24s was applied to avoid repeated fragmentation of the same precursor ions.

Mass Spectrum (MS) analysis

MS raw data was analyzed with Maxquant (v1.6.14)[42]. The main parameters were set as follow: the used database was from UniProt, enzyme specificity was set to 'Trypsin', allowing up to two missed cleavages; dynamic modifications were set at oxidation (M), fixed modifications were set at carbamidomethyl (C). Label-free quantification was enabled and 'Match between runs,' 'iBAQ' options were selected, then filtered by score was ≥ 20.

Protein information was obtained from "ProteinGroups.txt". For protein groups containing multiple matched proteins, the LFQ intensity of the group was used to represent the best matched protein.

For HeLa cells, the three replicates (acquired at different times and using different instruments) were first log2-transformed and then z-score standardized within each replicate, using the mean and standard deviation of intensities across all indicated chase time points. At each time point, the z-scores were then averaged across replicates. The heatmap displays the averaged z-scores of log2-transformed LFQ intensities. The ComBat function from sva package (v3.5) were used to correct batch effect between replicates.

For SH-SY5Y cells, four replicates were acquired on the same instrument with minimal technical variation. For downstream analysis, log2 transformation was performed on LFQ intensities, followed by calculation of the mean log2 LFQ intensity across

replicates. Protein-wise z-score standardization was then applied using the mean and standard deviation of mean log2 LFQ intensity across all chase time points.

For interpretation, a positive z-score indicates the protein abundance above the mean intensity across all indicated time points, whereas a negative z-socre indicates the protein abundance below the mean intensity. The abundance of sub-nucleolar localized proteins[2], SSU-[4] and LSU-[5] pre-rRNAs associated proteins were examined. For SSU- and LSU- pre-rRNA associated proteins at each indicated time point, the maximum z-score was defined as the peak enrichment of individual protein at the indicated chasing time. LOESS regression (span = 0.75) was performed in R (v4.3) to model the relationship between the z-score intensity dynamics across chase time of protein of interest.

RNA-seq library preparation and analysis

Total RNA was isolated from H9 (D0) and D30 differentiated arcuate neuron cells (D30). For each sample, the total RNA was processed for ribosomal RNAs depletion and library preparation with Illumina TruSeq® Stranded Total RNA LT Sample Prep Kit, and sequenced with Illumina NovaSeq 6000 system at Sequanta Technologies.

Fastqc (v0.11.9) was used to evaluate the quality of all raw reads and adapter-trimmed reads by Trimmomatics[43] (v0.32, parameters: TruSeq3-SE.fa:2:30:10 LEADING:3 TRAILING:3 SLIDINGWINDOW:4:15 MINLEN:30). Next, the reads were aligned to the human 45S rRNA reference (NR_046235.3) to further remove rRNA using Bowtie[44] (v1.1.2, parameters: -m 1 -k 1 -v 2 -S -p 12). The clean reads were aligned to hg38 using HISAT2[45] (v2.2.1, parameters: --no-softclip --rna-strandness RF --score-min L,-16,0 --mp 7,7 --rfg 0,7 --rdg 0,7 --max-seeds 20 -k 10 -t -p 12), and then converted to BAM files using samtools[46] (v1.6). Gene-level quantification was computed by featureCounts[47] (v2.0.1, parameters: -s 2 -p --fraction -O -T 16 -t exon -g gene_id).

Generated gene count matrix was subsequently loaded in R (v4.3) to identify differentially expressed genes using the package DESeq2[48] (v1.40.2). Next, we

retrieved 525 reported pre-rRNA processing factors according to literature, including factors related to pre-rRNA processing[11,49], genes annotated by Gene Ontology [50] (GO term "rRNA processing"), nucleolar proteins[2], SSU[4]- and LSU[5]- precursor associated proteins. 525 genes were further defined as upregulated (FC > 1.5, D30/D0; p.adjust < 0.01) or downregulated (FC < 0.67; p.adjust < 0.01) pre-rRNA processing factors.

ASOs treatment to inhibit pre-rRNA processing

For ASOs treatment, HeLa cells were seeded in 6-well plates, then the modified ASOs (3 μg/well) were transfected with Lipofectamine RNAiMAX Transfection Reagent (Invitrogen, 13778075) for 24 h before the subsequent assay.

smFISH in zebrafish embryos

Zebrafish embryos were injected EGFP-Fbl mRNA (400 ng/μL) at 1-cell stage to label the FZ region of zebrafish nucleoli, followed by 4 h incubation at 28 °C. Embryos were fixed with 4% PFA for 4 h at room temperature. Embryos were dehydrated with methanol and kept at -20 °C for over 2 h. After rehydration, the embryos were incubated in prehybridization buffer (10% formamide, 2×SSC, 0.1% Triton X-100) at 30 °C for 5min. Then the embryos were soaked in probe solution and incubated at 30 °C overnight in dark. On the following day, embryos were washed twice with prehybridization buffer at 30 °C for 30 min each and then briefly washed with PBST. Embryos were mounted with 1% agarose with DAPI and photographed using confocal microscopy (Olympus SpinSR)

Pulse labeling nascent RNAs with 5-EU in zebrafish embryos and HeLa cells

For pulse labeling nascent RNAs with 5-Eu in zebrafish embryos, we first injected EGFP-Fbl mRNA (400 ng/μL) into the embryos at 1-cell stage to label the FZ region of zebrafish nucleoli. At approximately 3 h incubation at 28 °C, when zygotic genome activation (ZGA) begins and endogenous rDNA starts transcription, we injected 5-EU (50 mM) into the yolk sac of zebrafish embryos to label nascent RNAs. Embryos were

733 then fixed at 10 min, 30 min, 60 min, 90 min and 180 min post 5-EU injection with 4%
734 PFA for 4 h at room temperature. Embryos were dehydrated with methanol and kept at
735 -20 °C for over 2 h. After rehydration, the embryos were incubated with the click
736 reaction mix (same as the mix in pulse-chase labeling combined with imaging in HeLa
737 cells) for 30 in at room temperature. Subsequently, embryos were rinsed two times with
738 PBST and photographed in 1% agarose gel using confocal microscopy (Olympus
739 SpinSR).

740 For pulse labeling nascent RNAs with 5-EU in HeLa cells, HeLa cells were cultured in
741 the medium supplemented with 1 mM 5-EU for 10 min, 30 min, 60 min, 90 min and
742 180 min. Next, cells were fixed with 4% PFA for 15 min at room temperature, followed
743 by permeabilization with 0.5% Triton X-100 for 10 min. The subsequent processes are
744 the same with the protocol of pulse-chase labeling combined with imaging.

745 **Calculating the Nascent Pre-rRNA Diffusion Rate**

746 The movement rate of nascent pre-rRNAs in HeLa, H9, SH-SY5Y, differentiated D30
747 arcuate neurons and ZF4 cells was calculated by examining the radial position of
748 maximal peak intensity at the sequential labeling time points. The absolute radial
749 distance corresponding to the maximal peak intensity over time represents the absolute
750 diffusion velocity. The radial position was subsequently normalized to the radius of
751 FBL signals. The normalized values were plotted against the indicated time points of
752 chase, resulting in the slope of the plot that indicates the relative diffusion rate. Linear
753 regression was applied to determine diffusion trends.

754 **Measurement of the ratio of the active rDNA**

755 To quantify the ratio of active rDNA in HeLa, H9, SH-SY5Y, differentiated D30
756 arcuate neuron cells, rDNA and RPA194 were co-stained and imaged by SIM as
757 described above. The 3D SIM image stacks were imported into Imaris software for
758 analysis. Briefly, (1) the rDNA signals and FC units (labeled by RPA194) were
759 segmented using custom functions as surface objects; (2) the integrated density of

rDNA signals within the total rDNA surfaces (I_{total}) and within the FC unit surfaces (I_{active}) were counted. The ratio of active rDNA was calculated as:

$$\text{Active rDNA} = \frac{I_{active}}{I_{total}}$$

Fitting of diffusion flux data

The radial position of the peak intensity of nascent pre-rRNA in each nucleolus, starting from the FC to the edge of the GC, was obtained via the plot profile analysis by ImageJ. The time-distance dataset was used to calculate the flow velocity and to fit the diffusion flux curve.

The temporal dynamics of relative diffusion flux were modeled using an exponential decay function. According to the simplified pre-rRNA flow model across nucleolar sub-compartments, the fitting process assumed that the relative diffusion flux *J(t)* at time *t* follows the equation:

$$J(t) = a \cdot e^{-b \cdot t} + c$$

where:

- *J(t)* represents the relative diffusion flux at time *t*,
- *a* is the amplitude of the initial flux,
- *b* is the rate constant that governs the exponential decay,
- *c* is the steady-state flux, representing the asymptotic value that the flux approaches as *t* increases.

The fitting was performed using the nonlinear least squares method through the *scipy.optimize.curve_fit* function in Python, which optimizes the parameters *a*, *b*, and *c* to minimize the residuals between the model and the experimental data.

Quantification and modeling of the Relative FC/DFC interface

To evaluate the physical and geometric interface between the FC and DFC within the nucleolus, we combined 3D image segmentation, contact area measurement, and mathematical modeling under spherical assumptions.

Individual FCs and DFCs were visualized by immunofluorescence labeling of the well-established markers RPA194 (FC) and FBL (DFC), followed by 3D reconstruction using Imaris (Bitplane). Each segmented FC and DFC surface was generated based on these markers, and the contact interface between them was quantified using the *XTension Surface–Surface Contact Area* function in Imaris. The primary surface was defined by the RPA194 signal (FC), and the secondary surface by the FBL signal (DFC) locally surrounding each FC. For each cell, the total FC/DFC interface area was calculated as the sum of all FC–DFC contact surfaces. The Relative FC/DFC interface is defined by normalizing each FC volume:

$$\text{Relative FC/DFC interface} = \frac{FC/DFC\ interface\ area}{FC\ volume}$$

To model the geometric relationship between the FC size and the contact interface, we assumed each FC as a spherical shape. The surface area and volume of such a spherical shape are given by, where r is the FC radius:

$$FC\ surface = 4\pi r^2$$

$$\text{FC Volume} = \frac{4}{3}\pi r^3$$

In some cells, FCs are not completely surrounded by DFCs. To account for this, we introduced a coverage correction factor α, representing the fraction of the FC surface in direct contact with the DFC, resulting in the formulas of the FC/DFC contact area:

$$FC/DFC \text{ interface area } = \text{ FC Surface} \times \alpha$$

Therefore, the theoretical Relative FC/DFC interface is:

$$Relative\ FC/DFC\ interface = \frac{FC/DFC\ interface\ area}{FC\ Volume} = \frac{3\alpha}{r}$$

When α = 1, the FC is assumed to be fully surrounded by DFC. $\alpha < 1$ reflects the partial DFC coverage.

In nucleolus with irregular FC morphology, the radius r is replaced by an effective radius reff to account for the non-spherical geometry.

$$Relative\ FC/DFC\ interface = \frac{3\alpha}{r_{reff}}$$

Fitting the curve of relative RNA intensity along the radial distance in pulse labeling assay.

The relative intensity of nascent pre-rRNAs along the radial distance was obtained by ImageJ. Data from 14 zebrafish embryos at each time point were plotted. Data from 15 FC/DFC units of more than 5 HeLa cells at each time point were plotted. The fitted relative intensity curve is obtained by Gaussian non-linear regression.

Animal use and care

All animal procedures were performed under the ethical guidelines of Center for Excellence in Molecular Cell Science, CAS.

Statistics and reproducibility

Statistical analyses were performed with Microsoft Office 365, GraphPad Prism 8, R (v4.3) and Python 3.8.8. For the sample size, statistical method and significance of all graphs, please see figure legends and methods for details. We used Student's t-test to analyze between-group differences. *P*-value < 0.05 was considered to indicate statistical significance. No data was excluded from the analysis. Microscopy imaging, northern blotting and western blotting were repeated independently at least three times with similar results.

Data availability

All data supporting the findings of this study are available in the Article and its Supplementary Information. RNA-seq data are available at the Gene Expression Omnibus under accession number GSE301874. Source data are provided with this paper.

Code availability

Custom code used in RNA-seq analysis in this study are available from https://github.com/YangLab/Pre-rRNA-spatial-distribution-and-functional-organization-of-the-nucleolus.

References

39 Wang, L., Egli, D. & Leibel, R. L. Efficient Generation of Hypothalamic Neurons from Human Pluripotent Stem Cells. *Curr Protoc Hum Genet* **90**, 21 25 21-21 25 14 (2016). https://doi.org:10.1002/cphg.3

40 Raj, A. & Tyagi, S. Detection of individual endogenous RNA transcripts in situ using multiple singly labeled probes. *Methods Enzymol* **472**, 365-386 (2010). https://doi.org:10.1016/S0076-6879(10)72004-8

41 Guo, X. *et al.* Capture of the newly transcribed RNA interactome using click chemistry. *Nat Protoc* **16**, 5193-5219 (2021). https://doi.org:10.1038/s41596-021-00609-y

42 Cox, J. & Mann, M. MaxQuant enables high peptide identification rates, individualized p.p.b.-range mass accuracies and proteome-wide protein quantification. *Nat Biotechnol* **26**, 1367-1372 (2008). https://doi.org:10.1038/nbt.1511

43 Bolger, A. M., Lohse, M. & Usadel, B. Trimmomatic: a flexible trimmer for Illumina sequence data. *Bioinformatics* **30**, 2114-2120 (2014). https://doi.org:10.1093/bioinformatics/btu170

44 Langmead, B., Trapnell, C., Pop, M. & Salzberg, S. L. Ultrafast and memory-efficient alignment of short DNA sequences to the human genome. *Genome Biol* **10**, R25 (2009). https://doi.org:10.1186/gb-2009-10-3-r25

45 Kim, D., Paggi, J. M., Park, C., Bennett, C. & Salzberg, S. L. Graph-based genome alignment and genotyping with HISAT2 and HISAT-genotype. *Nat Biotechnol* **37**, 907-915 (2019). https://doi.org:10.1038/s41587-019-0201-4

46 Li, H. *et al.* The Sequence Alignment/Map format and SAMtools. *Bioinformatics* **25**, 2078-2079 (2009). https://doi.org:10.1093/bioinformatics/btp352

47 Liao, Y., Smyth, G. K. & Shi, W. featureCounts: an efficient general purpose program for assigning sequence reads to genomic features. *Bioinformatics* **30**, 923-930 (2014). https://doi.org:10.1093/bioinformatics/btt656

48 Love, M. I., Huber, W. & Anders, S. Moderated estimation of fold change and dispersion for RNA-seq data with DESeq2. *Genome Biol* **15**, 550 (2014). https://doi.org:10.1186/s13059-014-0550-8

49 Dorner, K., Ruggeri, C., Zemp, I. & Kutay, U. Ribosome biogenesis factors-from names to functions. *EMBO J* **42**, e112699 (2023). https://doi.org:10.15252/embj.2022112699

50 Ashburner, M. *et al.* Gene ontology: tool for the unification of biology. The Gene Ontology Consortium. *Nat Genet* **25**, 25-29 (2000). https://doi.org:10.1038/75556

Acknowledgments

We thank members of the Chen laboratory for discussion; Sarah A. Woodson, Yi-Lan Chen and H. Wu for critical reading of our manuscript; the Narry Kim lab for providing the data of nascent RNAs bound proteins; L.-Z. Yang, M. L. Hou, B.-Y. Zou and D. Zhang for supporting our experiments. This work was supported by the Strategic Priority Research Program of the Chinese Academy of Science (XDB0570000), the National Key R&D Program of China (2021YFA1100203), the Postdoctoral Innovation Talent Support Program (BX20230362) and China Postdoctoral Science Foundation (2023M743481). This work has been supported by the New Cornerstone Science Foundation through the New Cornerstone Investigator Program. L.-L.C. is also a SANS Senior Investigator.

Author contributions

L.-L.C. supervised and conceived the project. L.-L.C., Y.-H.P. and L.S. designed experiments. Y.-Y.Z. performed computational analyses supervised by L.Y. and L.-L.C. Y.-H.P., L.S., performed all experiments and analyses with the help of Z.-H.Y., Y.Z., S.-M.C. X.-Q. L and J.Z. L.-L.C., Y.-H.P. and L.S. drafted the manuscript. L.-L.C. edited the manuscript.

Competing interests

L.-L. Chen is a co-founder of RiboX therapeutics. Other authors declare no competing interests.

Additional information

Supplementary Information is available for this paper. Correspondence and requests for materials should be addressed to L.-L. Chen. Reprints and permissions information is available at www.nature.com/reprints.

Figure 1. Spatiotemporal dissection of SSU and LSU pre-rRNA processing in the nucleolus.

a. 5' ETS-1 and 3' ETS probes detect 47S pre-rRNA (**Extended Data Fig. 1c**) at DFC and DFC/PDFC boundary, respectively. Top, probe positions. Bottom, averaged SIM images of 5' ETS-1, 3' ETS and FBL in HeLa cells. n = 33, 20 DFC units from 10, 11 cells, respectively.

b. smFISH probes targeting 5' ETS-2, 5' ETS-3 and ITS1 of SSU pre-rRNAs.

c. ITS1-detected SSU pre-rRNAs localize from FC/DFC border to PDFC.

d. Distinct 5' ETS segment distributions: 5' ETS-2 spans from FC to PDFC; 5' ETS-3 is confined to FC.

e. ITS2 (schematic, top)-detected LSU pre-rRNAs localize from PDFC to GC.

f. Distinct sub-nucleolar localizations of U17A and U8 snoRNAs. Top, schematic of target sites on pre-rRNAs. Bottom, representative images with FBL. n = 51, 58 DFC units from 13, 21 cells, respectively.

g. Distribution of detected pre-rRNA segments and snoRNAs across nucleolar subdomains. Top, averaged smFISH images of indicated pre-rRNA segments. n = 33, 42, 55, 57, 52, 20 DFC units, from 15, 15 ,15, 21, 15, 11 cells, respectively. Green circle marks FBL intensity peak. Bottom, relative radial intensity plots, shaded green area indicates DFC.

h. Averaged images of nascent pre-rRNAs (magenta) with FBL (green) and B23 (blue) over time. Nascent pre-rRNAs localize in FC-DFC (0-30 min) and extend into GC (40-60 min). n = 30 DFC units from 10 cells per condition.

i. Diffusion flux of pre-rRNAs decreases from nucleolar center to periphery. Fitting curve based on Extended Data Fig. 2d. Data are mean ± s.e.m., n = 20.

j. Heatmap of pre-rRNA-associated proteins dynamics: SSU-associated proteins enriched at 0-30 min, LSU-associated proteins at 60 min (full heatmap in **Extended Data Fig. 3c**).

k. Schematic summarizing the sequential spatial assembly of SSU and LSU.

Figure 2. Inefficient SSU pre-rRNA processing is associated with decreased FC/DFC interface and altered 5' ETS-3 localization.

a. Representative SIM images of nucleoli in H9 and differentiated D30 arcuate neuron cells, marked by FBL and RPA194.

b. Quantification of FC number and radius in (**a**), n = 45 cells.

c. Representative SIM images of nucleoli in HeLa and SH-SY5Y cells, marked by FBL and RPA194.

d. Quantification of FC number and radius in (**c**), n = 48 and 45 cells.

e. 5' ETS-3 localization shifts from FC-dominant (H9) to DFC-PDFC-dominant (D30 arcuate neuron and SH-SY5Y). Left, representative SIM images of 5' ETS-3 and FBL. Right, line intensity plot of 5' ETS-3 and FBL. n = 51 (H9), 11 (neuron), 23 (SH-SY5Y) DFC units from 15, 8, 10 cells, respectively.

f. NB of pre-rRNA intermediates during H9 neuronal differentiation, detected by 5' ETS-3 and ITS2 probes. Ethidium bromide (EB)-stained 18S and 28S serve as loading control.

g. Top, schematic of SSU and LSU pre-rRNAs detected by 5' ETS-3 and ITS2 probes. Bottom, quantification normalized to Day 0 in (**f**), showing 30S accumulation upon differentiation. n = 3 experiments.

h. 30S pre-rRNA accumulates in SH-SY5Y cells. Left, NB in HeLa and SH-SY5Y cells using 5' ETS-3 and ITS2 probes, with EB-stained 18S/28S as loading control. Right, quantification normalized to HeLa cells. n = 3 experiments.

i. Relative FC/DFC interface decreases in cells with inefficient SSU pre-rRNA processing. Left, schematic of FC/DFC unit size and interface. Right, quantification of Relative FC/DFC interface. n = 45 (H9), 45 (neuron), 48 (HeLa), and 45 (SH-SY5Y).

j. Proposed model illustrating nucleolar subdomain organization adapting to reduced ribosome biogenesis demands.

f, h, For gel source data, see **Supplementary Fig. 1**.

b, **d**, **g**, **h, i**, Data are mean ± s.e.m., two-tailed Student's t-test.

Figure 3. SSU pre-rRNA processing is critical for appropriate FC/DFC organization.

a. Representative averaged SIM images of nascent pre-rRNAs and FBL over chase times (0-60 min) in H9, SH-SY5Y and D30 arcuate neuron cells. n = 52, 50, 51, 50, 51, 51 (H9); 49, 38, 50, 57, 52, 50 (SH-SY5Y); 30, 30, 30, 33, 37, 32 (neuron) DFC units per time point. Scale bars, 500 nm.

b. Peak diffusion distances of nascent pre-rRNAs relative to FBL over time in HeLa, SH-SY5Y, H9 and D30 arcuated neuron cells. Data from averaged images in (**a**) and **Fig. 1h**. n = 20 (HeLa), 27 (H9, SH-SY5Y), and 25, 27, 26, 27, 27, 27 (neuron) DFC units per time point.

c. Schematic of ASOs targeting 5' ETS (ASO-Site A0, ASO-Site 1) and LSU (ASO-U8 Site, ASO-3' ETS) pre-RNA processing sites.

d. Left, NB of SSU (5' ETS-3) and LSU (ITS2) pre-rRNAs after ASO treatments. EB-stained 28S and 18S serve as loading control. Right, quantification of pre-rRNA intermediates (n=6, 3 for 5' ETS-3, ITS2 blots, respectively). For full gels, see **Supplementary Fig. 1**.

e. Impaired SSU, but not LSU pre-rRNA processing, remodels FC/DFC units. Left, representative SIM images of ASO-treated HeLa cells showing different FC/DFC patterns, indicated by FC (RPA194, magenta), DFC (DKC1, green) and GC (B23, blue). Right, schematic of major FC/DFC patterns under each treatment. See **Extended Data Fig. 8d** for additional patterns and proportions.

f. Statistics of FC/DFC reorganization after ASO treatment in (**e**). SSU pre-rRNA processing inhibition results in decreased Relative FC/DFC interface, reduced FC number, and enlarged FC size. Abnormal FC/DFC ratios are calculated from n = 6 experiments. Cell numbers n = 19, 21, 20, 27, 24 for each ASO treatment.

b, **e**, **g**, Data are presented as mean ± s.e.m., two-tailed Student's t-test.

Figure 4. Multi-layered nucleolus ensures highly efficient SSU pre-rRNA processing over bipartite nucleolus.

a. Spatial distribution of pre-rRNAs in the bipartite nucleolus of zebrafish ZF4 cells. Top, schematic of smFISH probe positions. Bottom, representative confocal images showing localization of different pre-rRNA segments. Z-Fbl (green) represents the FZ unit. Early pre-rRNA intermediates (5' ETS-1, 5' ETS-2 and ITS1) localize predominantly within FZ compartment and its vicinity.

b. Proposed model of the bipartite nucleolus displaying distinct pre-rRNA segment distributions.

c. Workflow of nascent pre-rRNAs labeling in zebrafish embryos.

d. Representative averaged images of nascent pre-rRNAs at indicated time points in zebrafish embryos. FZ unit numbers n = 58, 59, 59, 53, 52 per time point.

e. Representative averaged images of nascent pre-rRNAs at indicated time points in HeLa cells. FC/DFC unit numbers n = 34, 32, 36, 33, 32 per time point.

f. Nascent pre-rRNA outflux is reduced in bipartite nucleoli. Left, peak diffusion distance of nascent pre-rRNAs (magenta) over time in ZF4 cells. Fbl (green) serves as control. Right, relative peak diffusion distances comparing zebrafish and HeLa cells. Data are presented as mean ± s.e.m. FZ (or DFC) unit numbers n = 26, 39, 39, 42, 38, 37 (ZF4), and 20 (HeLa) per time point.

g. Proposed model comparing reduced nascent pre-rRNA outflux in bipartite nucleoli to higher flux in multi-layered nucleoli.

h. A proposed model illustrating how coordinated pre-rRNA processing, spatial distribution, and nucleolar substructure remodeling adapt to cellular physiology. In fast proliferating cells, SSU pre-rRNAs span across FC-PDFC regions, maintaining a high Relative FC/DFC interface for efficient 5' ETS processing with rapid SSU flux to meet cellular ribosome demands. In slowly growing cells, retarded SSU processing accompanies with remodeled FC/DFC substructures, reduced Relative FC/DFC interface and decreased SSU flux, reflecting a structure-function adaptation of nucleolar substructure to ribosome demands.

Extended Data Figure 1. Sub-nucleolar localization of pre-rRNA intermediates by designed smFISH probes.

a. Schematic of spatially organized nucleolar subdomains and corresponding steps of rRNA biogenesis. Transcription initiates in the FC, followed by modifications in the DFC, and processing with pre-ribosomal particle assembly in the PDFC and GC. The steps of pre-rRNA processing and RNP assembly are simplified.

b. Diagram summarizing pre-rRNA processing steps and intermediates. The smFISH probes used in this study are indicated in magenta, highlighting their target regions and the pre-rRNA intermediates expected to detect.

c. NB confirming 5' ETS-1 and 3' ETS probes mainly recognize the full-length 47S pre-rRNA. See also **Fig. 1a**.

d. The ITS1-targeted probe sets recognize the early-stage pre-rRNAs, including mostly 47S and some 41S pre-rRNAs. Representative images in (**g**) and **Fig. 1c**.

e. The 5' ETS-targeted probe sets recognize the early-stage pre-rRNAs and 18S rRNA precursors, including 47S and 30S pre-rRNAs. Representative images in **Fig. 1d**.

f. The ITS2-targeted probe sets recognize 5.8S/28S rRNA precursors. The probe ITS2 in **Fig. 1e** mainly recognizes the 32S and 12S pre-rRNAs. The probe spanning site 3' in (**h**) mainly recognizes the 32S pre-rRNA.

g. The Site 2 probe signals localize to the DFC – PDFC region. Left, probe schematic. Middle, representative single-slice and averaged SIM images of Site 2-detected 47S pre-rRNA (magenta) and FBL (green) in HeLa cells. Right, line intensity plot of Site 2 and FBL signals. n = 50 DFC units from 17 cells.

h. The Site 3'-detected LSU pre-rRNAs localize mainly to the PDFC-GC region. Left, probe schematic. Middle, representative single-slice and averaged SIM images of the Site 3'-detected 32S pre-rRNA (magenta) and FBL (green) in HeLa cells. Right, line intensity plot of Site 3' and FBL signals. n = 50 DFC units in 17 cells.

i. U13 snoRNA that binds the 3' end of 18S pre-rRNA is mainly localized to the DFC. Left, schematic depicting the targeted position of U13 snoRNA on the pre-rRNA. Middle, representative single-slice and averaged SIM images of U13 snoRNA (magenta) and FBL (green) in HeLa cells. Right, line intensity plot of U13 snoRNA and FBL signals. n = 53 DFC units from 10 cells.

j. E2 snoRNA that binds the 3' end of 18S pre-rRNA is largely localized to the DFC. Left, schematic depicting the targeted position of E2 snoRNA on the pre-rRNA. Middle, representative single-slice and averaged SIM images of E2 snoRNA (magenta) and FBL (green) in HeLa cells. Right, line intensity plot of E2 snoRNA

and FBL signals. n = 54 DFC units from 13 cells.

c,d,e,f, For gel source data, see **Supplementary Fig. 1**.

Extended Data Figure 2. Characterization of the kinetics of nascent pre-rRNAs.

a. The workflow of pulse-chase labeling experiment combined with super-resolution imaging and mass spectrometric (MS) analysis to examine the spatiotemporal distribution of SSU and LSU pre-rRNAs. Imaging tracks the pre-rRNAs outflux, while MS identifies nucleolar proteins associated with different stages of pre-rRNAs at indicated pulse-chase time points.

b. Relative pre-rRNAs intensities with radial position from the FC center over time, quantified from averaged images in **Fig. 1h**, showing a gradient outflux distribution of nascent rRNAs across nucleoli over time.

c. The peak diffusion distance of nascent pre-rRNAs over time (magenta), with the maximum intensity distance of FBL over time (green) as a DFC-localized control. The line is fitted with diffusion distance from DFC images in **Fig. 1h**. Data are mean ± s.e.m. n = 20 DFC units.

d. Schematic illustrating the pre-rRNA flow across nucleolar sub-compartments. Accompanying with the outward flow, pre-rRNAs are distributed in an increased 3D space, thus with a decreased spatial density. The relative diffusion flux is proportional to the density under the constant linear flow rate (calculated in (**c**)).

Extended Data Figure 3. Characterization of the nascent pre-rRNA associated nucleolar proteins.

a. Pearson's correlation of protein LFQ intensity from three MS repeats at each chase time point (0, 30, 60 min) after batch effect correction. The protein pull-down experiment was performed as described in **Extended Data Fig. 2a** in HeLa cells.

b. Dynamics of protein binding intensities across nucleolar subdomains. LOESS regression curves show averaged z-scores log2 LFQ intensities of proteins localized in FC, DFC, PDFC, and GC regions, respectively. The normalized log2 LFQ intensities were derived from three independent MS replicates.

c. Heatmap of SSU- and LSU- precursor-bound protein dynamics (0-, 30-, 60 min chase) in HeLa cells. SSU-precursor-bound proteins with peak enrichment time at early time points (0- and 30 min) and LSU-precursor-bound proteins with peak enrichment time at late time point (60 min) are marked by black boxes and highlighted in **Fig. 1j**. Values represent mean z-scores of log2-transformed LFQ intensities, first normalized within each replicate across time points and then averaged across three MS replicates.

d. Published time-resolved RNA interactome data using pulse-chase metabolic labeling with 4-thio-uridine also revealed a similar outflow pattern of nucleolar protein localization, consistent with the findings in this study: FC, DFC, and PDFC proteins bound nascent rRNAs sequentially within the first 40 min followed by GC proteins presented thereafter.

e. Top, schematic of the nucleolar sub-domains with representative marker proteins: FC (RPA194), DFC (FBL), PDFC (DDX21) and GC (B23). Bottom, Western blot (WB) analysis of proteins precipitated with 5-EU-labeled nascent pre-rRNAs in **Extended Data Fig. 2a** in HeLa cells. FBL is mostly enriched at the early chase time points (0 min and 30 min), DDX21 is mostly enriched at 30 min, and B23 is mostly enriched at 60 min mirroring the spatiotemporal distribution of nascent pre-rRNAs in **Fig. 1h**. For gel source data, see **Supplementary Fig. 1**.

f. The enrichment dynamics of representative proteins (RPA194, FBL, DDX21, and B23) in distinct nucleolar sub-domains (FC, DFC, PFDC, and GC) derived from MS data in HeLa cells. Values represent mean z-scores of log2-transformed LFQ intensities, first normalized within each replicate across time points and then averaged across three MS replicates. Results align with WB validation in (**e**).

g. A proposed model summarizing the spatial distribution patterns of distinct pre-rRNA segments and their association with SSU and LSU pre-ribosomes.

Extended Data Figure 4. Analysis of the altered FC/DFC interface in morphologically different nucleoli from different cells.

a. Number of FC/DFC units during H9 cell differentiation to arcuate neurons. Data are mean ± s.e.m. n = 31, 31, 31, 47, 33, 31, 31, 32 cells across the sequential time points.

b. Average FC volume in H9, D30 arcuate neurons, HeLa, and SH-SY5Y cells. Data are mean ± s.e.m. n = 45, 45, 48 and 45 cells, respectively. Statistical analysis was performed using two-tailed Student's t-test.

c. Visualization of the multi-layered nucleolar structure in D30 arcuated neurons. SIM images show the spatial organization of FBL (DFC, green) and B23 (GC, white), illustrating compartmentalized nucleolar subdomains.

d. Schematic and theoretical model for calculating the Relative FC/DFC interface. Left, regular and irregular FC/DFC structures are illustrated, with the FC/DFC contact area normalized to FC volume to define a relative interface. Middle, equations detail the derivation of the Relative FC/DFC interface for spherical or irregular FCs based on radius or effective radius (r or r_{reff}). Right, theoretical relationship showing the inverse correlation between Relative FC/DFC interface and FC radius.

Extended Data Figure 5. The spatial distribution of SSU pre-rRNAs in H9, D30 arcuate neuron and SH-SY5Y cells.

a. 5' ETS-1 localization in the DFC region remains consistent across different cell types. Left, schematic of the 5' ETS-1 probe position. Middle, representative single-slice and averaged SIM images of 5' ETS-1 (magenta) and FBL (green) in the indicated cell types. Right, the corresponding line intensity plots of 5' ETS-1 and FBL. n = 51, 12, 25 DFC units in 15 (H9), 10 (D30 arcuate neuron), 9 (SH-SY5Y) cells, respectively.

b. ITS1 localization in the DFC-PDFC regions remains consistent across different cell types. Left, schematic of the ITS1 probe position. Middle, representative single-slice and averaged SIM images of ITS1 (magenta) and FBL (green) in the indicated cell types. Right, the corresponding line intensity plots of ITS1 and FBL. n = 48, 27, 52 DFC units in 10 (H9), 12 (D30 arcuate neuron), 16 (SH-SY5Y) cells, respectively.

Extended Data Figure 6. The spatial distribution of different segments of LSU pre-rRNAs in H9, H9-differentiated D30 arcuate neurons and SH-SY5Y cells.

a. ITS2 localization in the PDFC-GC region remains unchanged across different cell types. Left, schematic of the ITS2 probe position. Middle, representative single-slice and averaged SIM images of ITS2 (magenta) and FBL (green). Right, the corresponding relative line intensity plots of ITS2 and FBL. n = 50, 22, 40 DFC units in 15 (H9), 10 (D30 arcuate neuron), 8 (SH-SY5Y) cells, respectively.

b. 3' ETS localization in the DFC-PDFC regions remains consistent across different cell types. Left, schematic of the 3' ETS probe position. Middle, representative single-slice and averaged SIM images of 3' ETS (magenta) and FBL (green). Right, the corresponding relative line intensity plots of 3' ETS and FBL. n = 52, 10, 50 DFC units in 14 (H9), 7 (D30 arcuate neuron), 13 (SH-SY5Y) cells, respectively.

Extended Data Figure 7. Reduced ribosome biogenesis and processing in post-mitotic cells.

a. Active rDNA loci are reduced in post-mitotic cells. Top, schematic of rDNA FISH probes. Bottom, representative images of rDNA (grey), FBL (green) and RPA194 (magenta) in H9, D30 arcuate neuron, HeLa and SH-SY5Y cells, showing active rDNA loci colocalizing with Pol I.

b. Top, quantification of active rDNA ratios per cell from (**a**), n = 12 (H9), 18 (neurons), 15 (HeLa), 27 (SH-SY5Y) cells. Bottom, schematic of rDNA organization in FC/DFC under altered proliferation rates.

c. Majority of pre-rRNA processing factors exhibit reduced expression during differentiation. Volcano plot showing differential gene expression (D30 arcuate neurons vs. H9) of 525 annotated pre-rRNA processing factors. Data was analyzed using three biological repeats. The p.adjust values were computed by DESeq2, which used a Wald test by default to calculate original p-values then adjusted for multiple testing using the Benjamini-Hochberg method.

d. Heatmap of SSU- and LSU-precursor- associated protein enrichment dynamics in SH-SY5Y cells. SSU-precursor-bound proteins with peak enrichment time at early time point (0- and 30 min) and LSU-precursor-bound proteins with peak enrichment time at late time point (60min) are marked by black boxes. Data was analyzed using four MS repeats performed as in **Extended Data Figure 2a** in SH-SY5Y cells. Mean log2 LFQ intensities were first averaged across four MS repeats and then z-score normalized across time points.

e. Delayed binding of SSU precursor associated proteins in SH-SY5Y cells. LOESS regression was performed on quantities of pre-rRNA-bound proteins and chase time points. The quantities of proteins were derived from MS data of HeLa (**Extended Data Fig. 3c**) and SH-SY5Y cells (**d**).

f. Proportion of pre-RNA-bound proteins enriched at early time points (0- and 30min) and at late time point (60 min) in HeLa (derived from **Extended Data Fig. 3c**) and SH-SY5Y cells (derived from panel (**d**)). Number of proteins is labeled on the bar.

g. Representative averaged SIM images of nascent pre-rRNAs over chase times (0-60 min) in H9, SH-SY5Y and D30 arcuate neuron cells. Each panel represents averaged signal from n = 52, 50, 51, 50, 51 and 51 DFC units per time point (H9 cells); 49, 38, 50, 57, 52 and 50 DFC units per time point (SH-SY5Y cells); 30, 30,

30, 33, 37 and 32 DFC units per time point (in D30 arcuate neurons). Scale bars, 500 nm.

Extended Data Figure 8. Blocking SSU pre-rRNA processing alters pre-rRNA spatial localization and FC/DFC unit organization.

a. Left top, ASOs incorporating phosphorothioate and 2'-MOE modifications. Representative SIM images showing the localization patterns of 5' ETS-3 (magenta) in ASOs-treated HeLa cells. FCs are labeled by RPA194 (blue) and DFC by DKC1 (green).

b. Representative SIM images showing normal and enlarged FC/DFC units. FCs are labeled by RPA194 (magenta), DFC by DKC1 (green), and GC by B23 (blue). Insets show magnified views of individual FC/DFC units.

c. Representative SIM images showing fragmented FC/DFC units in ASO-Site A0 and ASO-Site 1 treated cells.

d. Left, schematic illustration of three types of FC/DFC units: normal, enlarged and fragmented. Right, proportion of normal, enlarged, and fragmented FC/DFC units under each treatment condition. Data were obtained from n = 51, 27, 48 cells for ASO-Scr., ASO-Site A0, ASO-Site 1, respectively.

Extended Data Figure 9. Distinct nascent RNA kinetics in zebrafish and HeLa nucleoli.

a. Spatial organization of pre-rRNA segments in ZF4 cells and zebrafish embryos. Left, diagram of zebrafish pre-rRNA processing pathway with smFISH probe positions (magenta lines). Right, representative images showing localization of various pre-rRNA segments in ZF4 cells. Zebrafish Fbl (Z-Fbl, green) labels the FZ compartment. Probes targeting early processing intermediates (5′ ETS, ITS1, ITS2) show signal enrichment within or adjacent to the FZ, while probes targeting mature sequences (18S and 28S) primarily label transcripts in the outer granular zone (GZ), indicating a spatial separation of early and late processing steps.

b. Representative averaged images of nascent pre-rRNAs (magenta) and Fbl (green) at the sequential labeling time points in zebrafish embryos. Fbl marks the FZ. See also **Fig. 4d**.

c. Representative averaged images of nascent pre-rRNAs (magenta) and FBL (green) at sequential labeling time points in HeLa nucleoli. FBL marks the DFC. See also **Fig. 4e**.

d. Representative whole-nucleus images of nascent pre-rRNAs and Fbl in zebrafish embryos with quantification of nascent rRNA intensities at different time points (right), n = 13, 12, 22, 15, 11cells over time points.

e. Representative whole-nucleus images of nascent pre-rRNAs and FBL in HeLa cells with quantification of nascent rRNA intensities at different time points (right), n = 15 cells per time point.

d, e Curves are fitted using one-phase association. The stable intensity of Pol II-transcribed nascent RNAs (nucleoplasm distributed) over the continuous labeling period excludes the possibility that 5-EU exhaustion can cause the reduced nascent pre-rRNA signals within the innermost FC region.

Extended Data Figure 10. Multi-layered nucleoli exhibit functional advantages in pre-rRNA processing over bipartite nucleoli.

a. Representative whole-nucleus images of nascent pre-rRNAs (magenta) and zebrafish Fbl (green) in ZF4 cells at indicated chase time points (0–90 min). Scale bars, 5 μm.

b. Radial distribution of pre-rRNA intensities (relative to Fbl center) in zebrafish embryos at indicated time points from **Fig. 4d.**

c. Radial distribution of pre-rRNA intensities (relative to FBL center) in HeLa cells at indicated time points from **Fig. 4e**.

d. Human TCOF1 overexpression (OE) induces tripartite-like nucleoli in ZF4 cells and accelerates pre-rRNA outflux. Top, workflow of TCOF1 OE and subsequent 5-EU pulse-chase assay in ZF4 cells. Bottom, representative images of nascent pre-rRNAs (firefly), z-Fbl (green), and TCOF1 (magenta) at indicated time points in wild-type (ZF4-WT) and TCOF1-OE ZF4 cells. Scale bars, 2 μm.

e. Top, schematic of the induced tripartite-like nucleolar architecture in TCOF1-OE cells with enhanced FC/DFC-like segregation. Bottom, time-course of normalized nascent pre-rRNA signal intensity across chase intervals in WT and TCOF1-OE ZF4 cells. Data were obtained from n = 26, 39, 42 and 38 cells in WT; 14, 7, 19 and 7 cells in TCOF1-OE. Data are mean ± s.e.m.

b and **c**, the curves are fitted with Gaussian non-linear regression. n = 15.

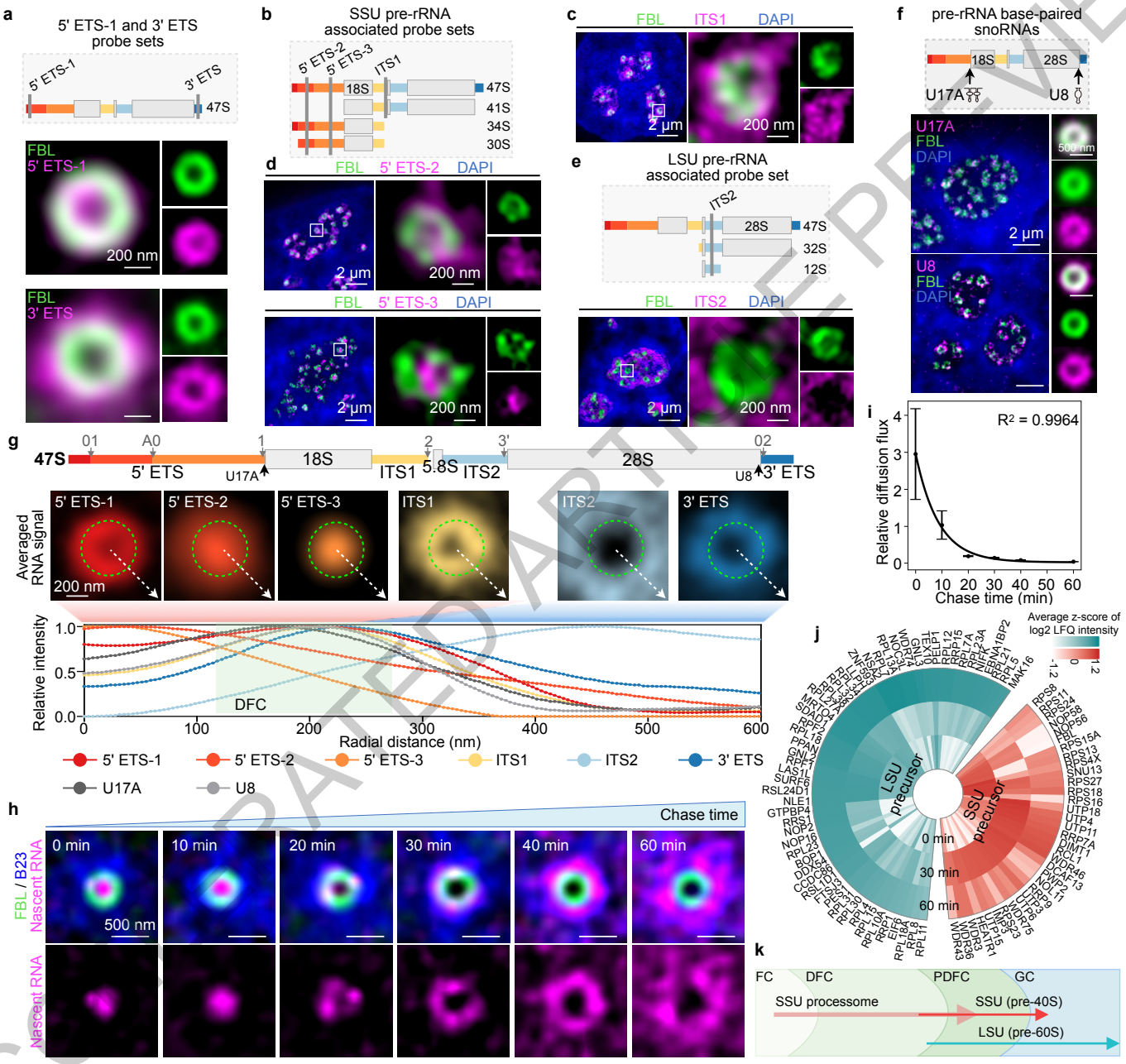
a
5' ETS-1 and 3' ETS probe sets
5' ETS-1
3' ETS
47S
FBL
5' ETS-1
200 nm
FBL
3' ETS
b
SSU pre-rRNA associated probe sets
5' ETS-2
5' ETS-3
ITS1
18S
47S
41S
34S
30S
c
FBL
ITS1
DAPI
2 μm
200 nm
d
FBL
5' ETS-2
DAPI
2 μm
200 nm
FBL
5' ETS-3
DAPI
2 μm
200 nm
e
LSU pre-rRNA associated probe set
ITS2
28S
47S
32S
12S
FBL
ITS2
DAPI
2 μm
200 nm
f
pre-rRNA base-paired snoRNAs
18S
28S
U17A
U8
U17A
FBL
DAPI
500 nm
2 μm
U8
FBL
DAPI
g
47S
01
A0
1
2
3'
02
5' ETS
U17A
18S
ITS1
5.8S
ITS2
28S
U8
3' ETS
Averaged RNA signal
5' ETS-1
5' ETS-2
5' ETS-3
ITS1
ITS2
3' ETS
200 nm
Relative intensity
1.0
0.5
0.0
DFC
0
100
200
300
400
500
600
Radial distance (nm)
5' ETS-1
5' ETS-2
5' ETS-3
ITS1
ITS2
3' ETS
U17A
U8
i
R² = 0.9964
Relative diffusion flux
4
3
2
1
0
0
10
20
30
40
50
60
Chase time (min)
j
Average z-score of log2 LFQ intensity
-1.2
0
1.2
LSU precursor
SSU precursor
0 min
30 min
60 min
h
Chase time
FBL / B23
Nascent RNA
0 min
10 min
20 min
30 min
40 min
60 min
500 nm
Nascent RNA
k
FC
DFC
PDFC
GC
SSU processome
SSU (pre-40S)
LSU (pre-60S)

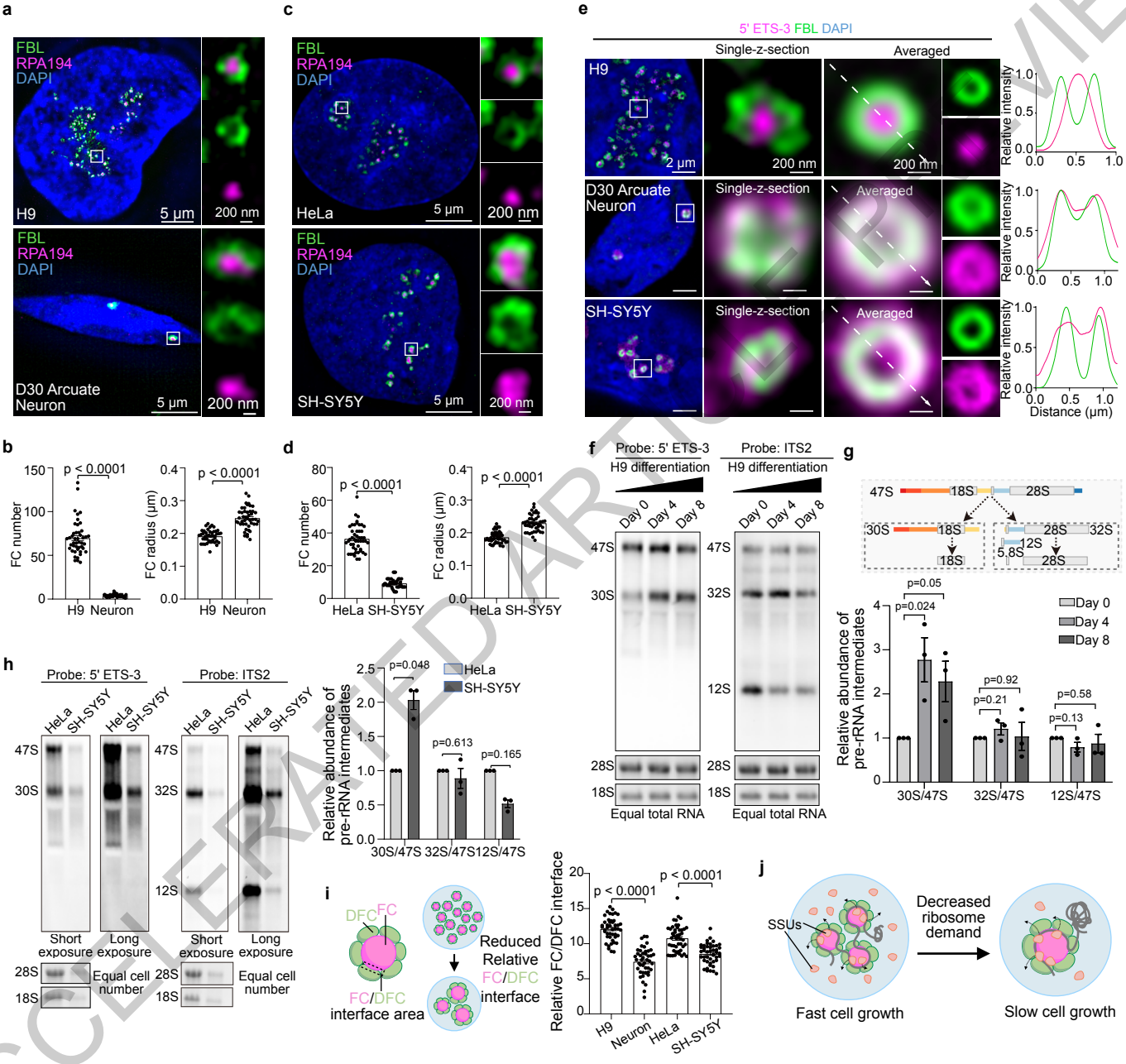

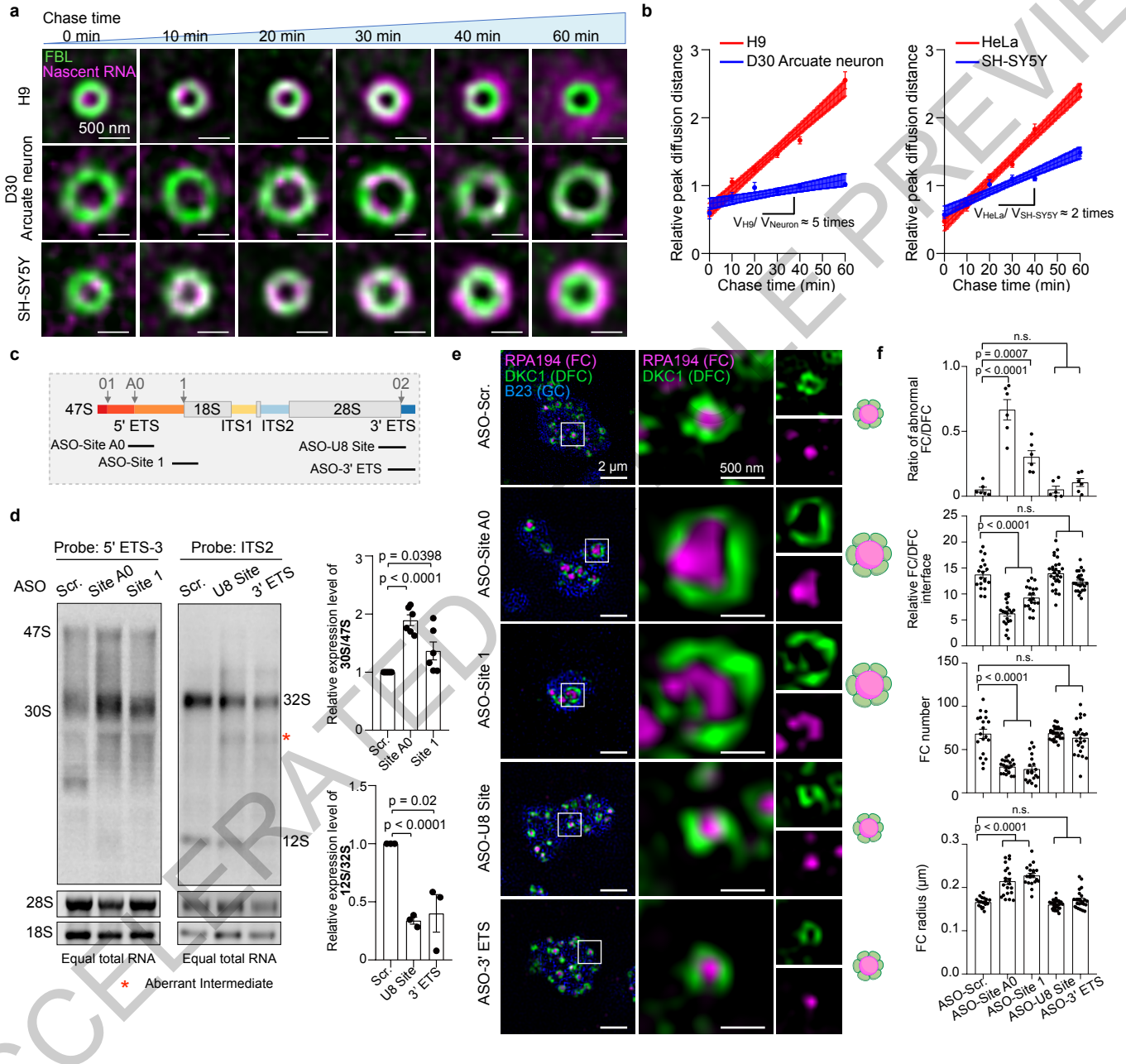

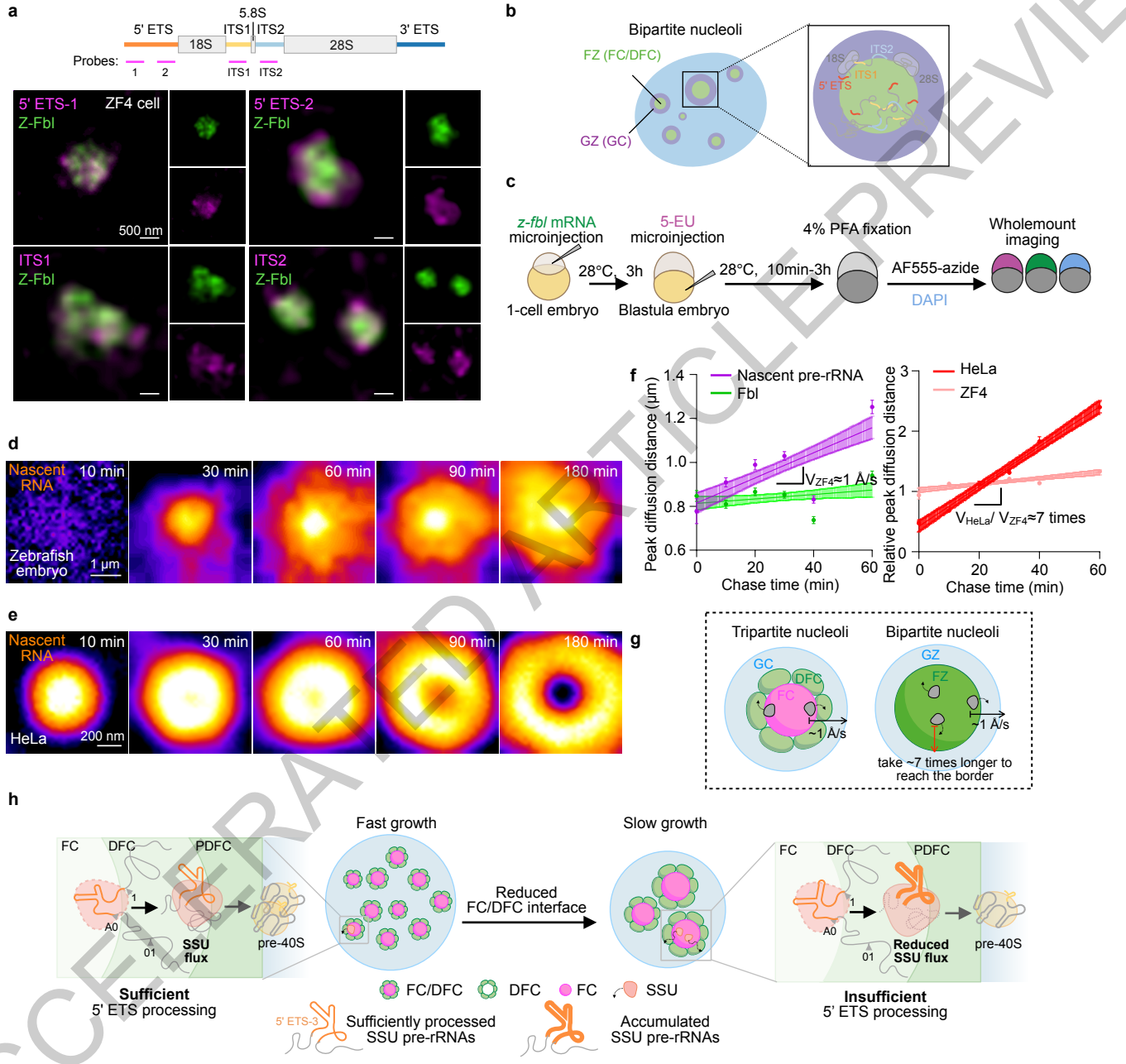

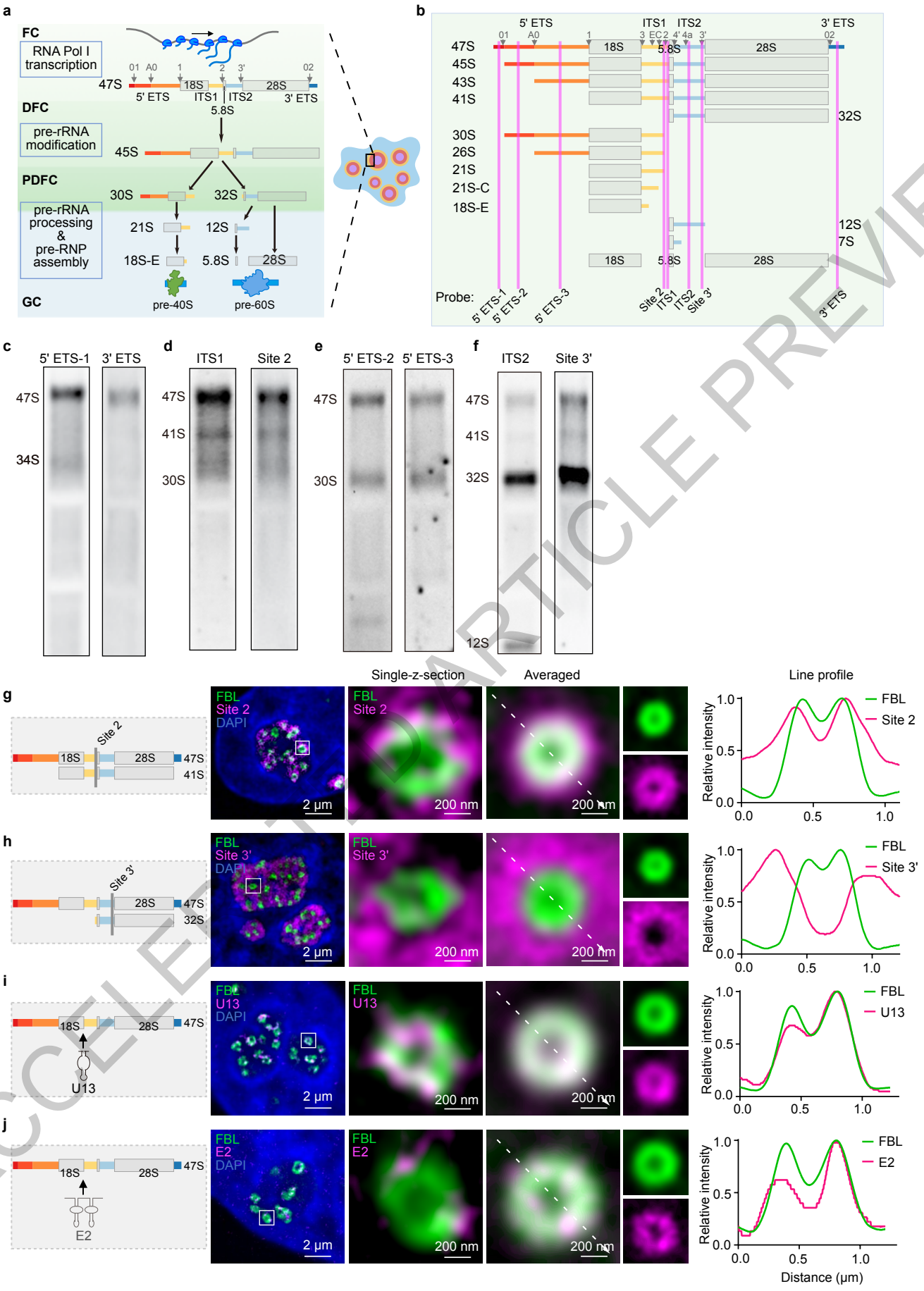

Extended Data Fig. 1

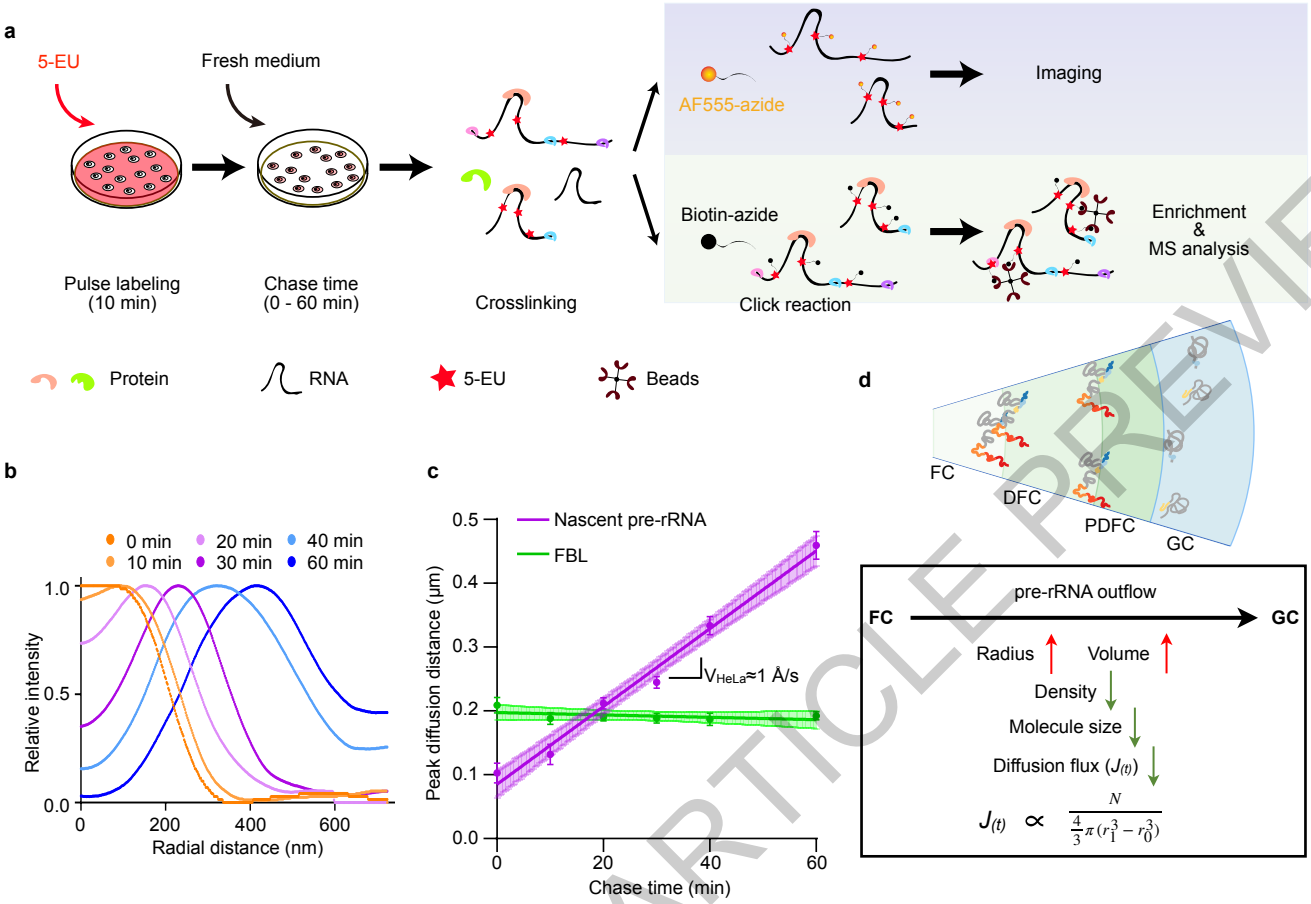

Extended Data Fig. 2

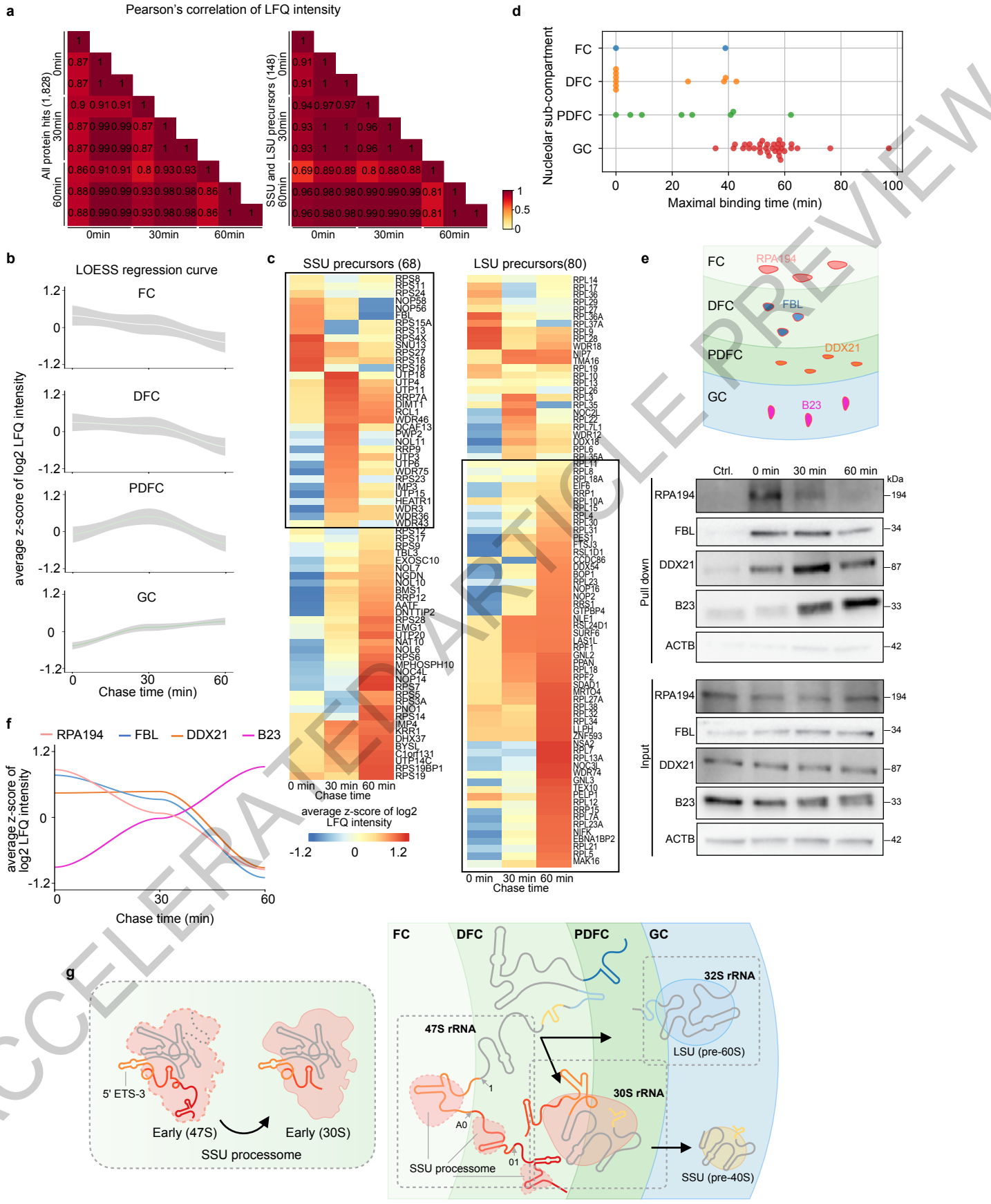

Extended Data Fig. 3

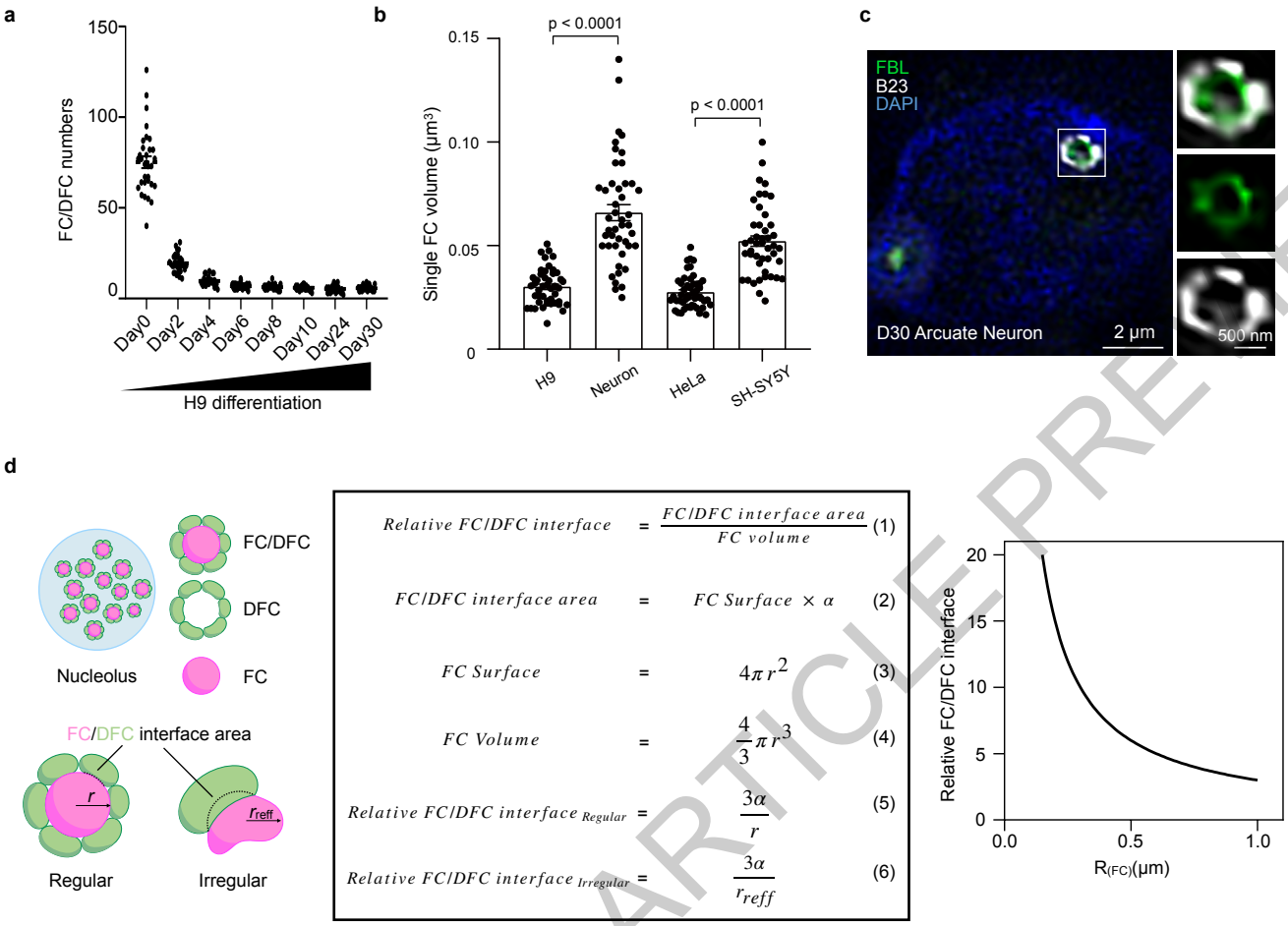

Extended Data Fig. 4

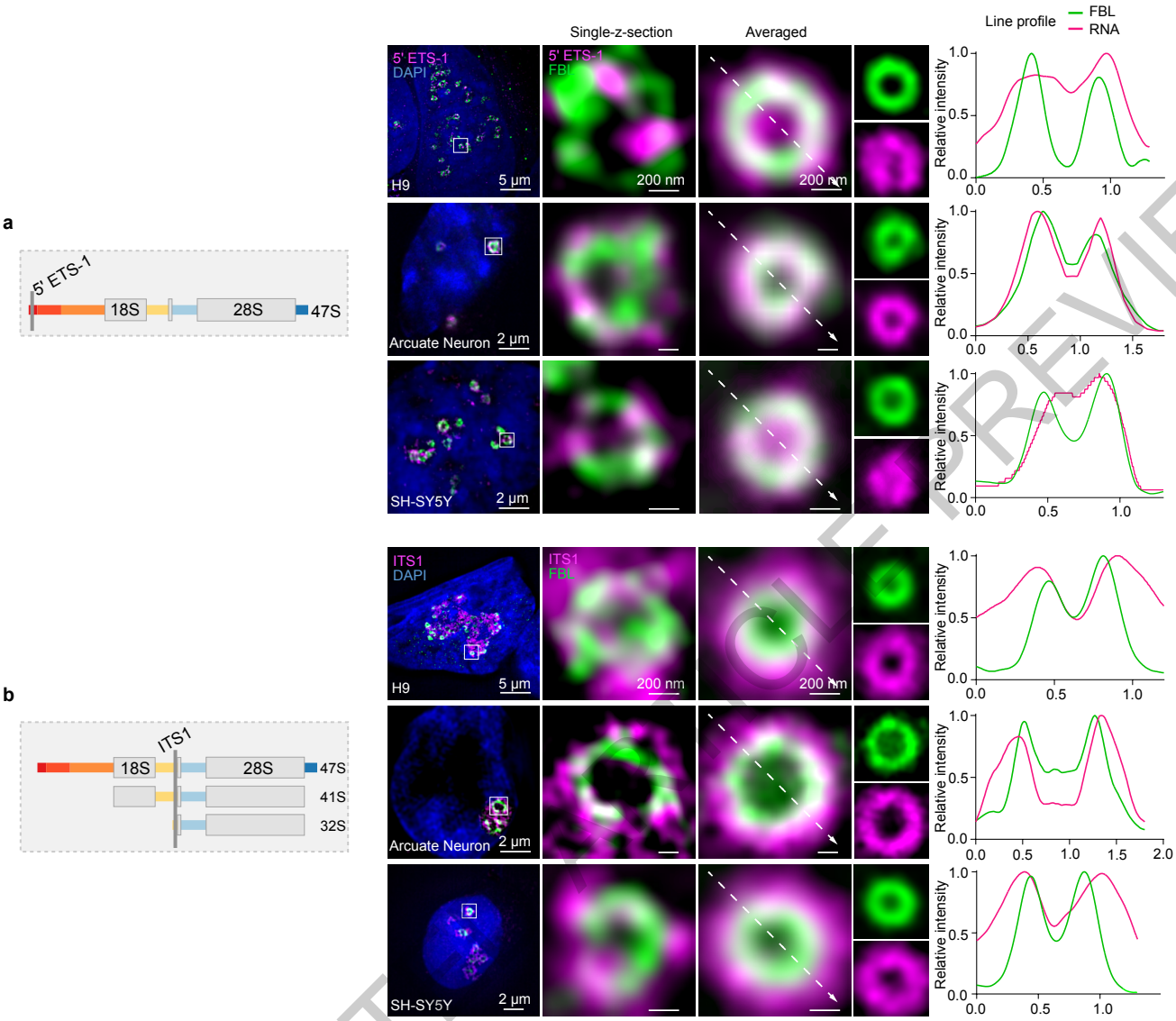

Extended Data Fig. 5

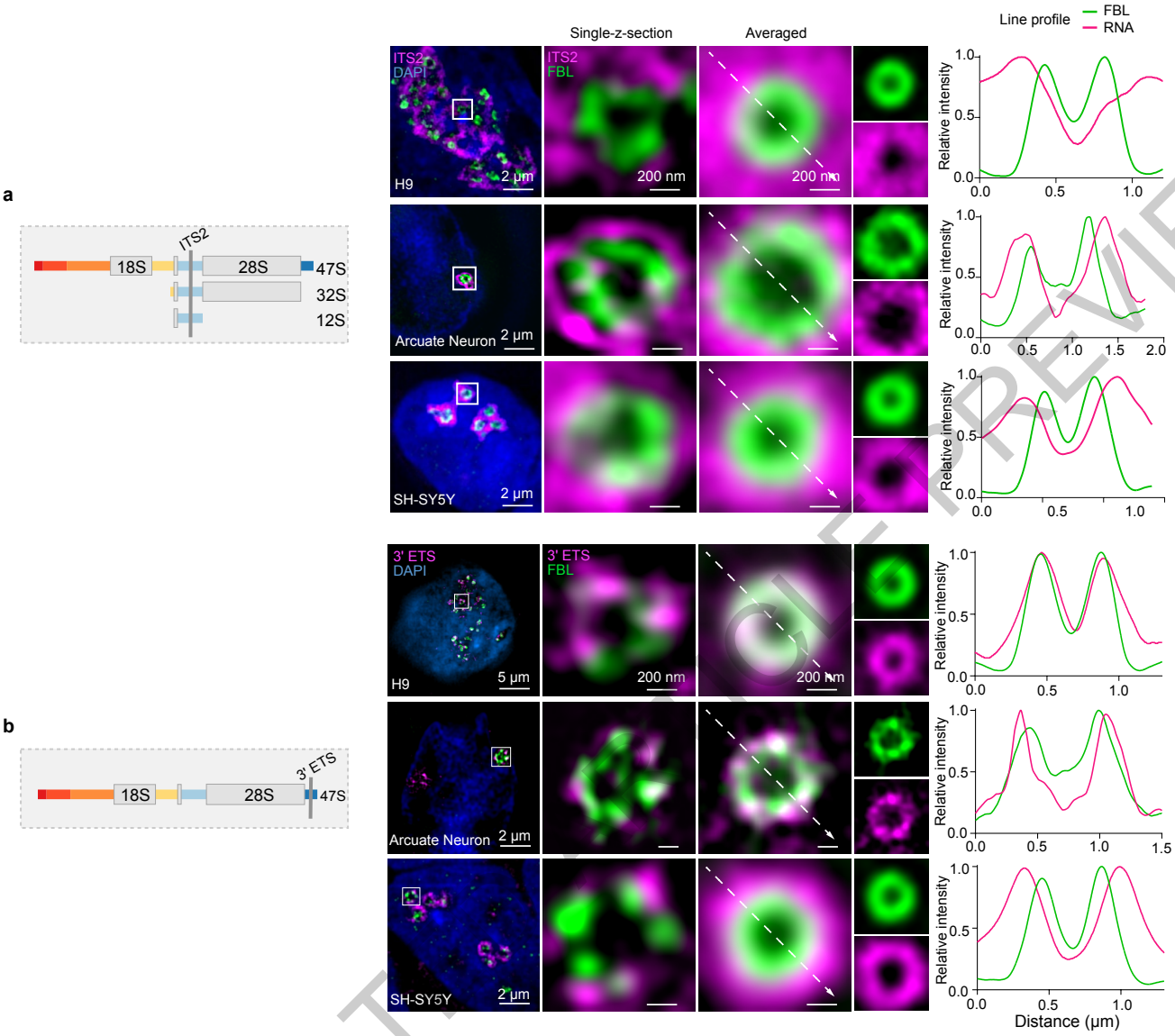

Extended Data Fig. 6

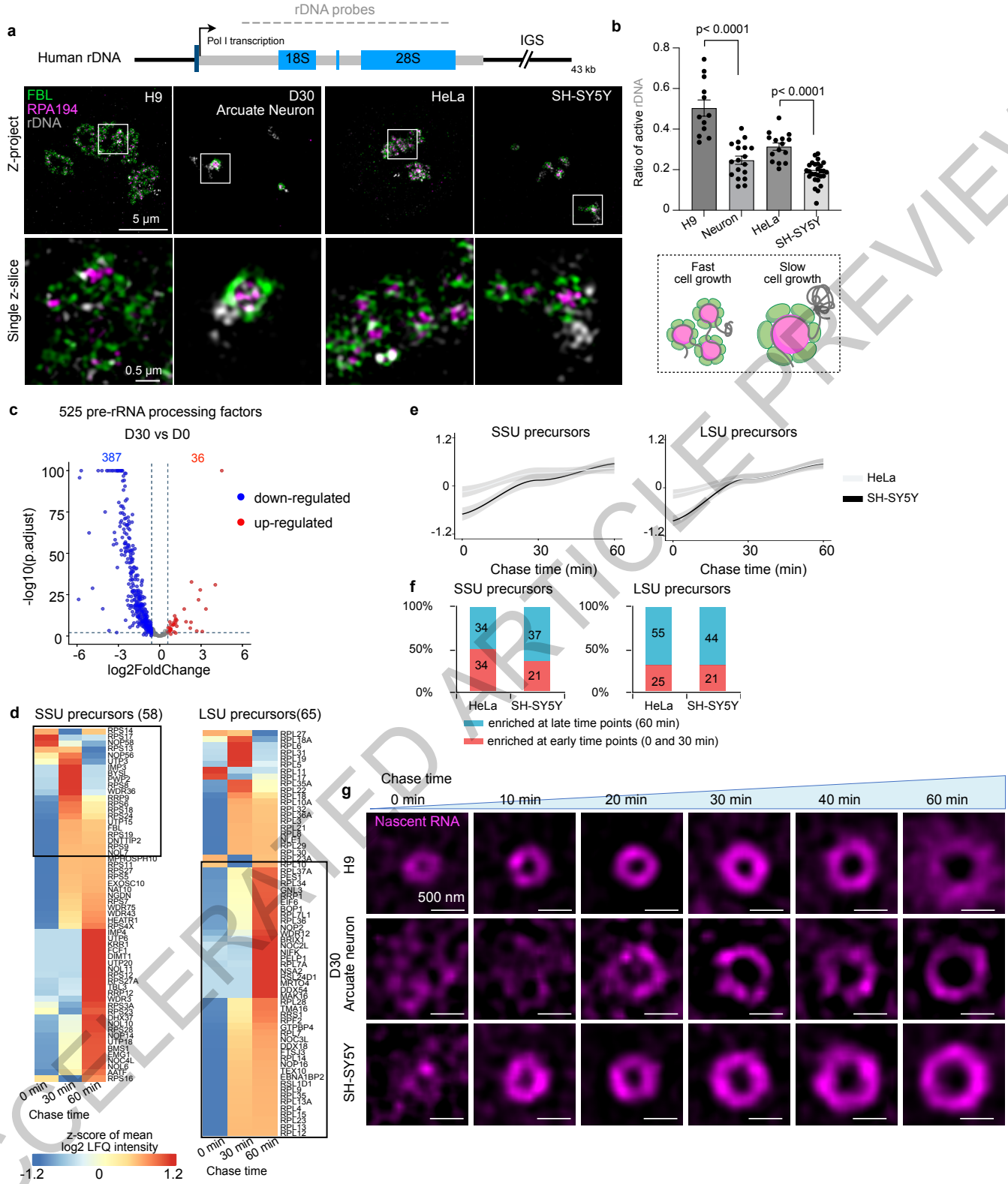

Extended Data Fig. 7

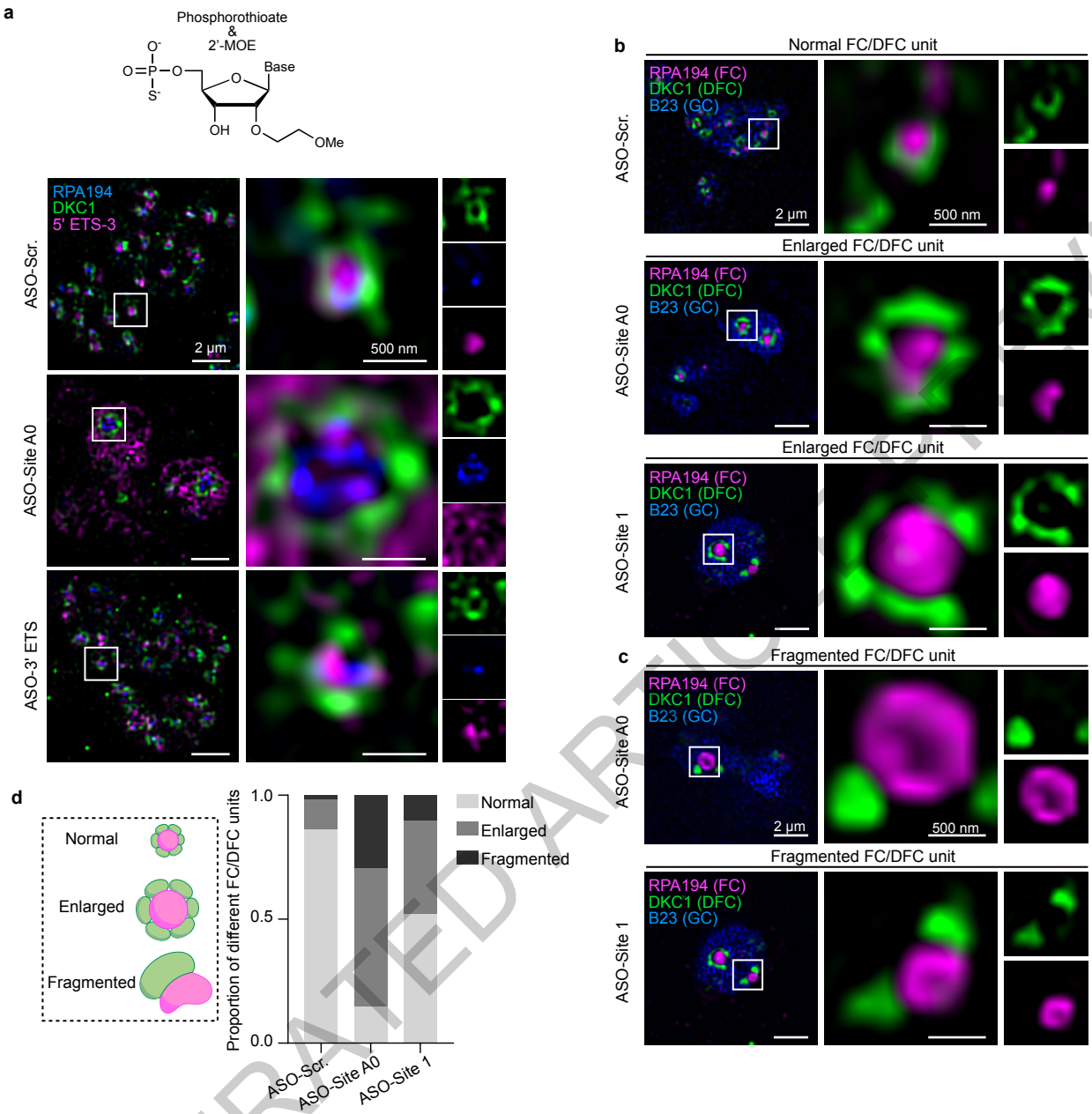

Extended Data Fig. 8

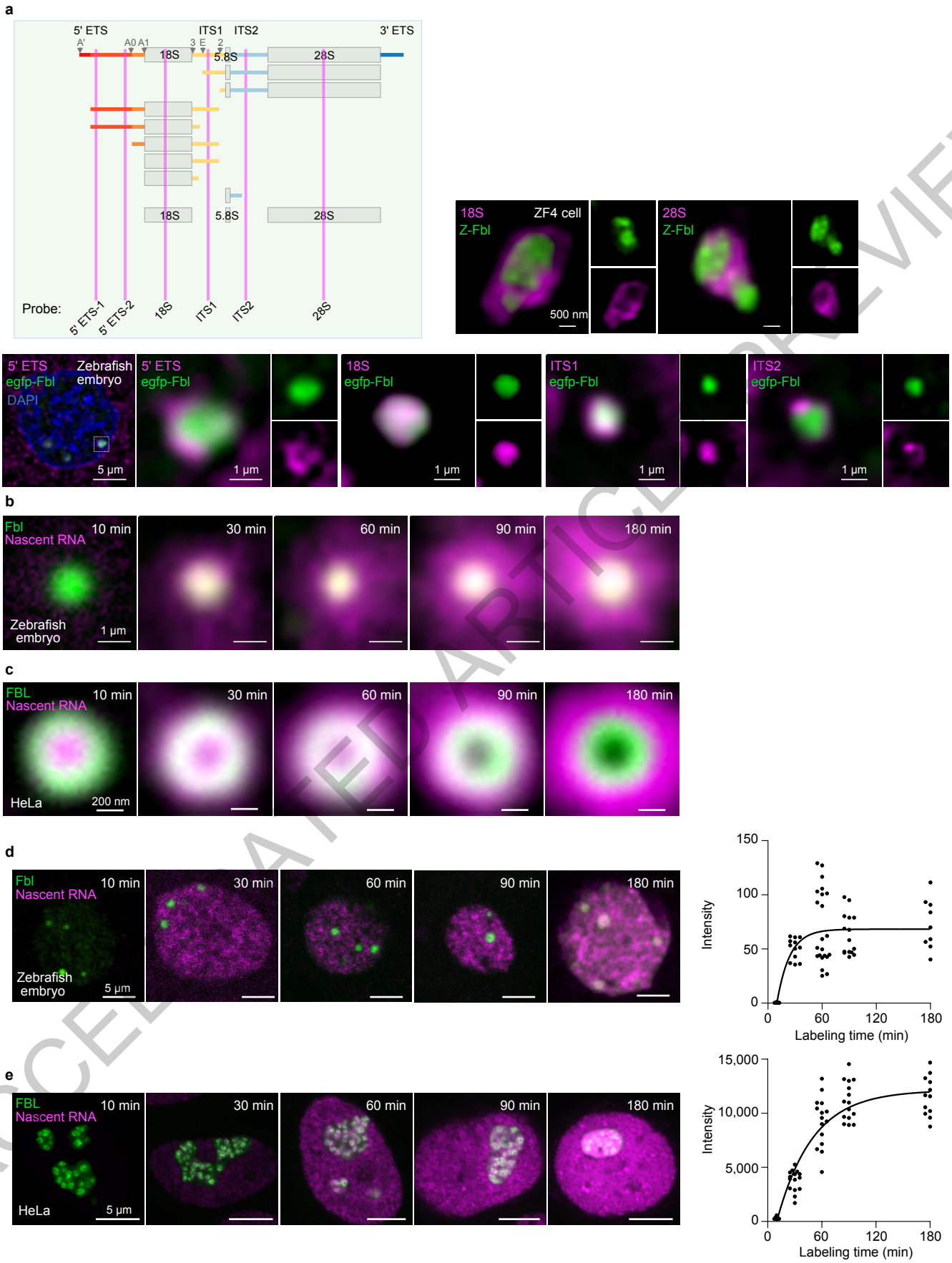

Extended Data Fig. 9

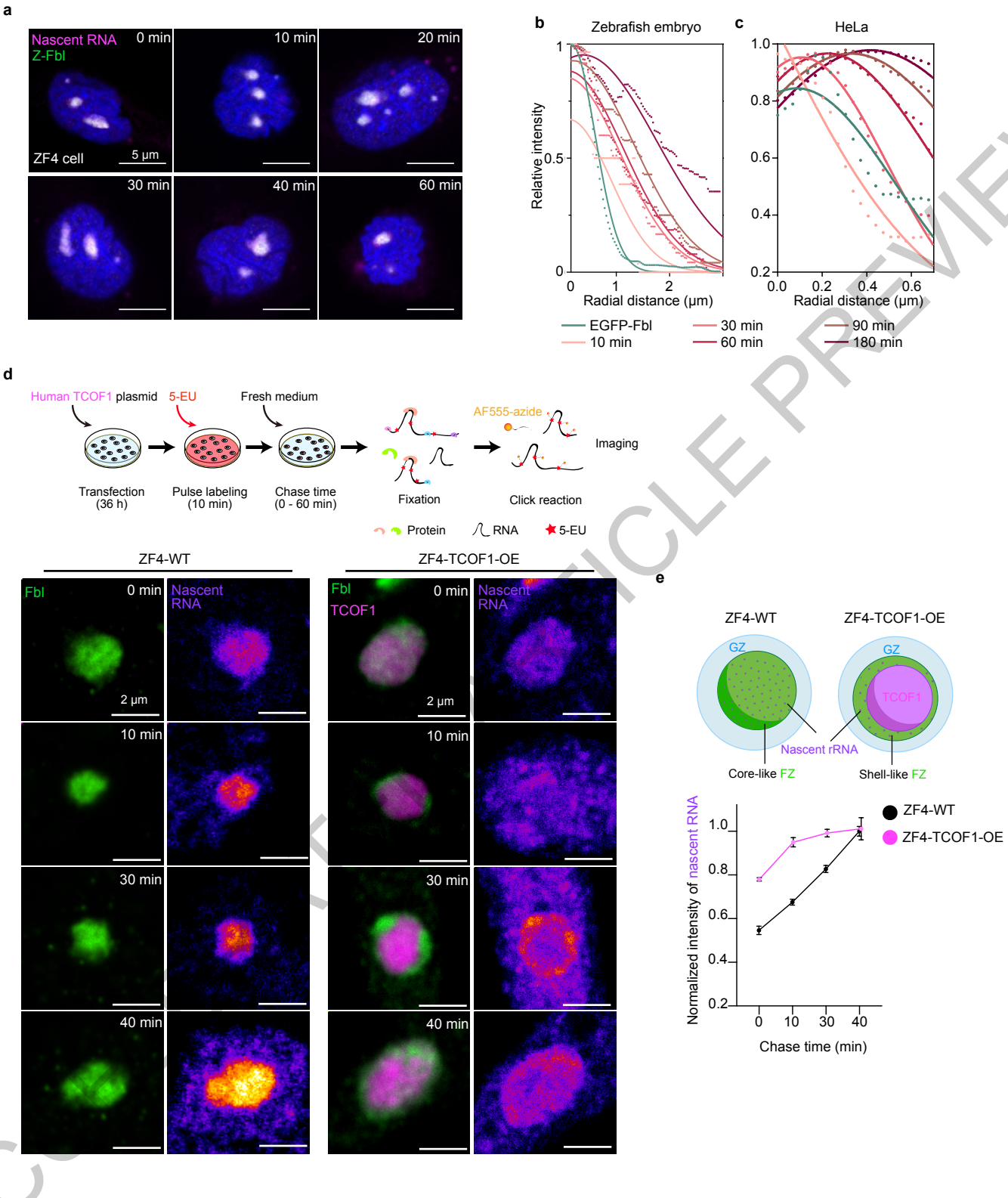

Extended Data Fig. 10

nature portfolio

Corresponding author(s): Ling-Ling Chen

Last updated by author(s): Jul 10, 2025

Reporting Summary

Nature Portfolio wishes to improve the reproducibility of the work that we publish. This form provides structure for consistency and transparency in reporting. For further information on Nature Portfolio policies, see our Editorial Policies and the Editorial Policy Checklist.

Statistics

For all statistical analyses, confirm that the following items are present in the figure legend, table legend, main text, or Methods section.

n/a	Confirmed
☐	☒ The exact sample size (*n*) for each experimental group/condition, given as a discrete number and unit of measurement
☐	☒ A statement on whether measurements were taken from distinct samples or whether the same sample was measured repeatedly
☐	☒ The statistical test(s) used AND whether they are one- or two-sided *Only common tests should be described solely by name; describe more complex techniques in the Methods section.*
☐	☒ A description of all covariates tested
☒	☐ A description of any assumptions or corrections, such as tests of normality and adjustment for multiple comparisons
☐	☒ A full description of the statistical parameters including central tendency (e.g. means) or other basic estimates (e.g. regression coefficient) AND variation (e.g. standard deviation) or associated estimates of uncertainty (e.g. confidence intervals)
☐	☒ For null hypothesis testing, the test statistic (e.g. *F*, *t*, *r*) with confidence intervals, effect sizes, degrees of freedom and *P* value noted *Give P values as exact values whenever suitable.*
☒	☐ For Bayesian analysis, information on the choice of priors and Markov chain Monte Carlo settings
☒	☐ For hierarchical and complex designs, identification of the appropriate level for tests and full reporting of outcomes
☐	☒ Estimates of effect sizes (e.g. Cohen's *d*, Pearson's *r*), indicating how they were calculated

Our web collection on statistics for biologists contains articles on many of the points above.

Software and code

Policy information about availability of computer code

Data collection	SIM images were acquired with IMAGER software (1.4.21c) and VSIM (2.2.1.10). Spin disk images were acquired with cellSens (3.1).
Data analysis	For imaging analyses, Fiji Image J (ImageJ 1.53c) and Imaris (9.0) were used. GraphPad Prism9, R (v4.3) and Microsoft office 365 were used for statistical analysis and graphing. MS raw data was analyzed with Maxquant 1.6.14. The main parameters were set as follow: the used database was from UniProt, enzyme specificity was set to 'Trypsin', allowing up to two missed cleavages; dynamic modifications were set at oxidation (M), fixed modifications were set at carbamidomethyl (C). Label-free quantification was enabled and 'Match between runs,' 'iBAQ' options were selected. The ProteomicsTools is 3.1.6. The filter by score was ≥ 20. Protein information was obtained from "ProteinGroups.txt". For protein groups containing multiple matched proteins, the LFQ intensity of the group was used to represent the best matched protein, and the z-score of log2 intensity of each protein across samples was calculated. We used the nucleolar protein sub-nucleolar localization dataset, SSU-associated protein dataset and LSU-associated protein dataset as three curated datasets. By comparing with these databases, 90 proteins with precise sub-nucleolar localization, 55 SSU-associated proteins and 60 LSU-associated proteins were found in our MS data. For each nucleolar sub-compartment localized proteins, LOESS regression (span = 0.75) was performed in R (v4.3) to model the relationship between the z-score intensity and each chase time. The Combat function from sva package (v3.5) were used to correct batch effect between replicates.

For manuscripts utilizing custom algorithms or software that are central to the research but not yet described in published literature, software must be made available to editors and reviewers. We strongly encourage code deposition in a community repository (e.g. GitHub). See the Nature Portfolio guidelines for submitting code & software for further information.

Data

Policy information about availability of data

All manuscripts must include a data availability statement. This statement should provide the following information, where applicable:

- Accession codes, unique identifiers, or web links for publicly available datasets
- A description of any restrictions on data availability
- For clinical datasets or third party data, please ensure that the statement adheres to our policy

All data supporting the findings of this study are available in the manuscript, Supplementary Data and Source Data. RNA-seq datasets are available in GEO (GSE301874).

Research involving human participants, their data, or biological material

Policy information about studies with human participants or human data. See also policy information about sex, gender (identity/presentation), and sexual orientation and race, ethnicity and racism.

Reporting on sex and gender	N/A
Reporting on race, ethnicity, or other socially relevant groupings	N/A
Population characteristics	N/A
Recruitment	N/A
Ethics oversight	N/A

Note that full information on the approval of the study protocol must also be provided in the manuscript.

Field-specific reporting

Please select the one below that is the best fit for your research. If you are not sure, read the appropriate sections before making your selection.

☒ Life sciences ☐ Behavioural & social sciences ☐ Ecological, evolutionary & environmental sciences

For a reference copy of the document with all sections, see nature.com/documents/nr-reporting-summary-flat.pdf

Life sciences study design

All studies must disclose on these points even when the disclosure is negative.

Sample size	Preliminary experiments were performed to determine the sample size. Sample size sufficiency were determined by previous experiments from our laboratories. No statistical methods were used to predetermine the sample size.
Data exclusions	No data was excluded.
Replication	Embryos were collected from at least 10 pairs of fish breedings. Data come from at least two independent experiments. All replication experiments gave similar results. All samples were pulled together during analysis.
Randomization	For the zebrafish experiments: embryos were allocated into experimental groups based on different treatments. For cell experiments: cells were allocated into experimental groups based on different culture conditions or ASO treatments.
Blinding	Not applicable due to the lack of randomizable treatments/interventions in the experimental plan.

Reporting for specific materials, systems and methods

We require information from authors about some types of materials, experimental systems and methods used in many studies. Here, indicate whether each material, system or method listed is relevant to your study. If you are not sure if a list item applies to your research, read the appropriate section before selecting a response.

Materials & experimental systems

n/a	Involved in the study
☐	☒ Antibodies
☐	☒ Eukaryotic cell lines
☒	☐ Palaeontology and archaeology
☐	☒ Animals and other organisms
☒	☐ Clinical data
☒	☐ Dual use research of concern
☒	☐ Plants

Methods

n/a	Involved in the study
☒	☐ ChIP-seq
☒	☐ Flow cytometry
☒	☐ MRI-based neuroimaging

Antibodies

Antibodies used

1) anti-FBL (Abcam; ab5821)
2) anti-RPA194 (Santa Cruz; sc-48385)
3) anti-B23 (Santa Cruz; sc-53175)
4) anti-DDX21 (Proteintech; 10528-1-AP)
5) anti-ACTB (Sigma; A3854)
6) anti-Digoxigenin-AP, Fab fragments (Roche; 11093274910)
7) Goat anti-Mouse Secondary Antibody, Alexa Fluor 555 (Invitrogen; A-21424)
8) Goat anti-Mouse Secondary Antibody, Alexa Fluor 647 (Invitrogen; A-27040)
9) Goat anti-Rabbit Secondary Antibody, Alexa Fluor 488 (Invitrogen; A-11034)

Validation

These antibodies have been widely used by other researchers worldwide or be validated by the vendor. FBL rabbit polyclonal antibody (Abcam; ab5821) is validated for immunofluorescent and WB analysis by previous experiments from our laboratories. RPA194 mouse monoclonal antibody (Santa Cruz; sc-48385) is validated for Immunofluorescent and WB analysis (manufacture's website). B23 mouse monoclonal antibody (Santa Cruz Biotechnology; sc-53175) is validated for Immunofluorescent analysis in HeLa cells (The EMBO Journal (2015) 34:2758-2774). DDX21 polyclonal antibody (Proteintech; 10528-1-AP) is validated for Immunofluorescent and WB analysis (manufacture's website). Anti-b-Actin-HRP conjugated primary antibody (Sigma; A3853) is validated for WB analysis at 1:10000 dilution (Cancer research, 72(10), 2645-2656 (2012-04-12); Cell reports, 28(7), 1703-1716 (2019-08-15)).

Eukaryotic cell lines

Policy information about cell lines and Sex and Gender in Research

Cell line source(s)

Cell lines are from commercial sources.
HeLa and SH-SY5Y cell lines were purchased from ATCC
Human H9 cell line was purchased from WiCell
ZF4 cell line was purchased from Yaji Biological

Authentication

Vendors of the commercially-obtained cell lines (ATCC/WiCell/Yaji Biological) provide further information on the generation, characteristics and authentication of the cell lines in their website, respectively.

Mycoplasma contamination

All cell lines were tested for free of mycoplasm contamination.

Commonly misidentified lines
(See ICLAC register)

No lines used in this study were found in the database of commonly misidentified cell lines that is maintained by ICLAC.

Animals and other research organisms

Policy information about studies involving animals; ARRIVE guidelines recommended for reporting animal research, and Sex and Gender in Research

Laboratory animals

Zebrafish embryos: sex of the embryos was not determined. To obtain embryos, pairs of female and male adult zebrafish (8-12 months old) were mated. Injections of EGFP-Fbl mRNA were performed at the one-cell stage. After mRNA injection, embryos were incubated for 3 hours prior to 5-EU injection.

Wild animals

No wild animals were used in the study.

Reporting on sex

Sex of the embryos was not determined

Field-collected samples

No field-collected samples were used in the study.

Ethics oversight

All animal procedures were performed under the ethical guidelines of the CAS Center for Excellence in Molecular Cell Science, Chinese Academy of Sciences (CAS).

Note that full information on the approval of the study protocol must also be provided in the manuscript.

Plants

Seed stocks	N/A
Novel plant genotypes	N/A
Authentication	N/A